Roads Prescription Scale Effectiveness Monitoring Project

Biennial Report for the Washington State Department of Natural Resources

June 2021

Charlie Luce[1], Tom Black[1], Amanda Manaster[2], Erkan Istanbulluoglu[2], Julie Dieu[3], Bob Danehy[4], Jenelle Black[5], Teresa Miskovic[6], Heather Gibbs[6]

[1]U.S. Forest Service, [2]University of Washington, [3]Rayonier, [4]Catchment Aquatic Ecology, [5]Northwest Indian Fisheries Commission, [6]Washington State Department of Natural Resources

Contents

Executive Summary

This interim report presents results from the Roads Prescription Scale Effectiveness Monitoring Project for the 2019-2021 biennium. Preliminary results are available from the 2019-2020 water year from the Major Experiment investigating road sediment production. The U.S. Forest Service is reporting the interim results from the Major Experiment and the University of Washington is reporting the interim results from the Ditch-Line Hydraulics and Micro-Topography Experiments, as well as progress in constructing the road sediment model, although major contributions have been made by all partners in this work. Specific accomplishments include the following:

- The preliminary sediment results from the Major Experiment support a conceptual model of sediment-production-limited behavior at most sites.
- Limitations in the sediment site flow monitoring equipment have been substantially resolved with the updating of equipment and installation of weirs at 10 of the higher flow sites.
- A model to calculate traffic effects on sediment availability was developed and will provide guidance for design of the Short-Time-Scale Interactions experiment.
- The first Ditch Line Hydraulics parameterization experiment was completed in May 2021, and initial calculations indicate the relative effectiveness of grass and wattles in the ditch line in providing immobile roughness to reduce ditch sediment transport capacity.
- The Micro-Topography experiment shows the evolution of small changes in the road surface driven by erosion and traffic.

Project Background

Forest roads provide many functions such as transportation of timber products, emergency access, and access for recreationists, hunters, and fishermen. At the same time, road erosion is a source of anthropogenic sediment in watersheds managed for timber production. Fine-grained sediment has the potential to adversely affect water quality and aquatic resources at the site, channel reach, and watershed scales.

Increased inorganic sediment loads, beyond quantities or frequencies that occur naturally, can influence the stream biota in many ways. Turbidity can reduce stream primary production by reducing photosynthesis, which affects other organisms in the food web. In addition, turbidity impacts gill function and respiration, and limits feeding success of fish. Deposited sediments may affect fish or amphibians directly by smothering eggs in redd or oviposition sites, altering spawning or early rearing habitat, and reducing overwintering habitat for fry. Fish or amphibians may also be affected indirectly by deposited sediments that limit invertebrate species composition, thereby decreasing abundance of preferred prey (Suttle et al., 2004).

Recognizing that roads are persistent sources of fine sediment to forest streams, forest managers have made substantial improvements in water quality in recent decades through their diligent application of best management practices (BMP). Cross-drain culverts to relieve ditch water before it reaches a stream crossing have become a common practice. Based on a first-time sampling of road BMP, initial monitoring results in western Washington indicate that 10-11% of the total forested road length directly delivers sediment to the channel network. This 10-11% of the total forest road length is stream-adjacent, cannot be successfully drained onto a hillslope, and, where this situation coincides with heavy traffic, leads to increased delivery of sediment to streams (Dubé et al., 2010).

A focal question in this project is: *What combinations of surfacing, ditch line management, traffic control, and drainage management will most efficiently and effectively mitigate sediment yields from high-traffic, near-stream (HTNS) roads*? Many previous studies have tested individual BMP, but landowners are more likely to implement multiple BMP simultaneously (e.g., it is common to reconstruct an old road by adding better quality rock, increasing the number of cross-drain culverts, putting the tread into a crowned configuration, and grassing the ditch line). Thus, studying multiple BMP as a set is a logical approach. In fact, one BMP may even reduce the effectiveness of another one. For example, paving a road reduces sediment delivered from the surface but contributes more water to the ditch line and, if the ditch is bare soil, erosion can increase relative to that expected in a ditch adjacent to a gravel road.

HTNS roads are important to the transportation network as key mainline roads, but they are more likely to deliver sediment to streams. To meet stewardship goals and effectively address operational needs, HTNS roads warrant additional investment by landowners to increase BMP beyond those in common use.

Road upgrades and enhanced BMP, however, can incur a significant cost. Therefore, improved knowledge of both the effectiveness of individual and integrated combinations of BMP is useful for understanding the return on BMP investments.

1 Major Experiment

1.1 Objectives

Three main treatment variables are being investigated for the Major Experiment: lithology (volcanic or siltstone), rock quality (good—the best locally available rock—or marginal—a lower quality rock that is locally available but that a landowner would use on a forest road with significant haul), and ditch line BMP (vegetated, bare, or elevated). Elevated BMP are structures like check dams or wattles, and one or more elevated BMP will be selected for testing during future years of the study.

During the first four years of the study, per the study plan (CMER, 2017), half of the sites are treated with marginal rock and the other half are treated with good rock in both lithologies. The variables of traffic loading, observed rainfall, and watershed contributing area are being measured for use as covariates. The variables of road length (80 m), width (3.66 m), road slope (2.5-13%), and construction type are being controlled (Table 1.1).

Table 1.1 *Additional potential covariates in the examination of BMP performance (CMER 2017).*

Covariate	Measured/Controlled	Measurement	Range/Condition
Segment Length	Controlled	---	Steel troughs and cross-drains isolate 80-m road segment
Tread Configuration	Controlled	---	Graded to a crown
Road Width	Controlled	---	Crest graded 3.66 m from ditch line
Road Gradient	Measured	---	Limited to 2.5-13%
Traffic	Measured	Inductance Loop Traffic counters, Motion-sensing cameras	Heavy traffic (4+ log trucks per day)
Grading	Measured	Landowner reporting and motion-sensing cameras	---
Rainfall	Measured	Rain gauges	Hourly precipitation
Catchment Area	Measured	Mapping catchment area above segment cut slope	---
Cut slope Interception	Measured/Estimated	Ditch line flow observations compared to hourly rainfall minus estimated tread contribution	---

1.2 Study Areas

The study sites were selected to include high traffic mainline forest roads in regions that receive heavy winter rainfall. The selected areas typically receive an average annual precipitation of 60-100 inches or more (PRISM, 2017). Groups of roads selected in the western portion of the study area occur on fine-grained sedmentary lithologies which are referred to as the siltstone province. These include sites on the Delezenne, Melbourne, Newskah, Bishop and Naselle road systems (Figure 1.1). Sites selected on the Kid Valley road system and the South Fork Toutle mainline exist on volcanic lithologies and are referred to as the volcanic province. Road segments were selected on private timberland roads that had planned log haul during the course of the study.

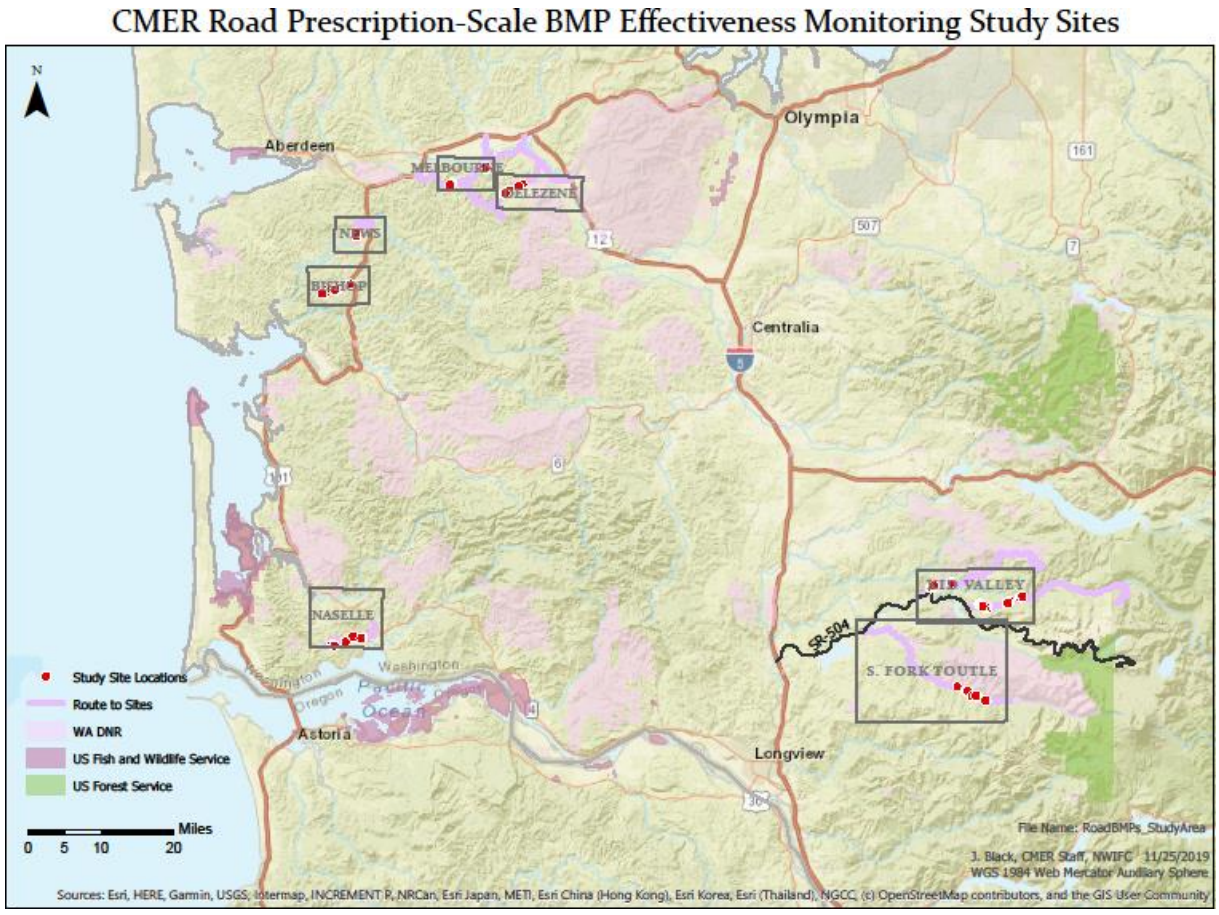

Figure 1.1 *Locations of the HTNS Major Experiment sites in western Washington.*

1.3 Methods

We constructed 78 sites, targeting specifically HTNS roads—39 in each of the two lithologies with overlapping ranges of rainfall typical of forested land in Western Washington. Each site consists of an 80-meter segment of road with a cut slope, a ditch line, and a road tread surfaced with crushed rock of either good or marginal quality (Figure 1.2). These sites exist in multiple clusters within each lithology. We installed a rain gage near each cluster to track local precipitation. In addition to the rain gages, we have installed traffic counters near site clusters and road junctions. These traffic counters and nearby motion-sensor cameras give us data regarding how much traffic these sites are seeing during a given month.

Figure 1.2 *"Good" rock (i.e., relatively unweathered basalt) is the darker rock in this picture, and "marginal" rock (i.e., slightly more weathered) appears with a lighter tan color. Good rock is used at most sites in practice, and marginal rock has been applied at approximately one-half of the sites to test the effects of rock quality on sediment yield.*

The tread surface of each 80-meter segment of road is isolated by steel troughs. The upper end of the ditch line of each segment is isolated by a cross-drain culvert with an earthen headwall. The cross-drain culvert passes the ditch and road tread water captured by the upper steel trough under the forest road and onto the forest floor. This ensures that the sediment collection equipment is only collecting water from the 80-meter segment. At the lower end of each 80-meter segment, the lower steel trough directs the water from the ditch-side tread crown (3.66 m from the ditch line) into the ditch. Water collected in the ditch from the cut slope and the 80 meters of crowned tread passes through the lower cross-drain culvert under the road to the sediment collection equipment (Figure 1.3 and Figure 1.4).

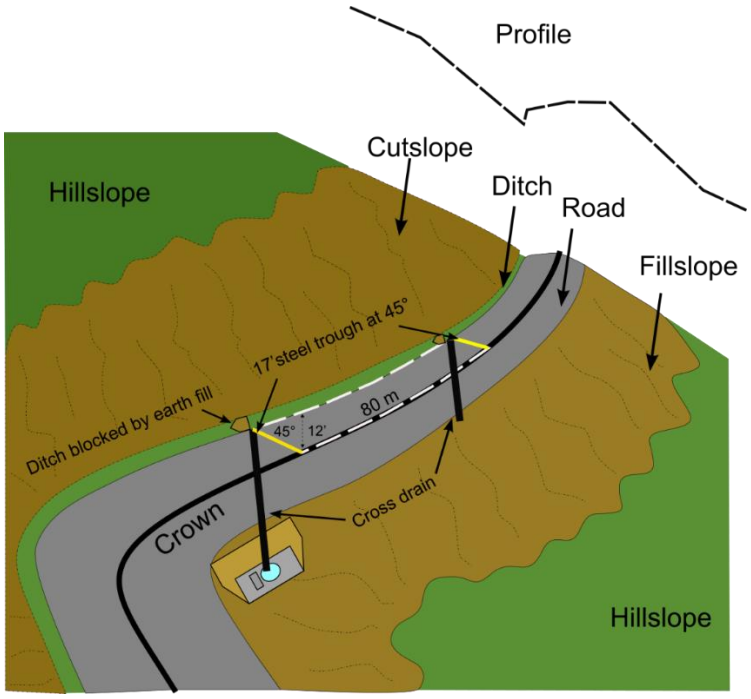

Figure 1.3 *Configuration of an 80-meter segment. Ditch (in green) is blocked below each cross-drain culvert by earthen headwall. Steel trough is 5.2 m-long and placed on a 45-degree angle up the road to capture 3.66 m of the crowned road tread and drain into the ditch line .3 m above each cross-drain culvert inlet. The lower cross-drain culvert is on a strong skew to create a 5% gradient in the pipe, and it extends several feet beyond the edge of the tread to a platform that holds the sediment tub, tipping bucket and SST.*

Figure 1.4 *The upper image shows the road surface routing water to the ditch and the collection trough. Water and sediment then are routed through a culvert pipe to the sediment tub platform. The lower image shows the sediment tub platform with the sediment tub collecting road sediment, the tipping bucket measuring discharge, and the suspended-solids tank (SST) sampling the fine sediment that is not settled in the sediment tub.*

On a 200 ft^2 platform dug into the fill slope or hillslope below the road, road sediment collection equipment collects both larger sized sediment (i.e., primarily sand) and finer material (i.e., the turbid fraction) with different methods. The cross-drain culvert that is located at the bottom end of the site will move water and sediment that is captured from the road and ditch line within the site into a tub that collects sediment at the outlet of the cross-drain culvert. The larger particles will accumulate in the sediment tub (developed by Black and Luce, 2013). Water exiting the sediment tub will pass through a tipping bucket with a data logger, measuring total water flow from the sediment tub. Finer suspended sediment escaping the sediment tub is sampled with every other tip of the tipping bucket. During these alternate tipping bucket tips, a 10-ml sub-sample of discharge is captured in a small pipe with holes mounted on one wall of the tipping bucket. This sub-sample of water and suspended sediment is routed to the suspended solids tank (SST) located below the tipping bucket where the finer sediment accumulates until field crews collect samples.

Field visits occur at all sites at least monthly during the rainy season (i.e., October to April). Samples are taken by 1) downloading the data logger to determine the discharge of water and 2) resuspending the sediment in the SST through mechanical mixing by a crew member and taking a one-liter representative sample thereof. SST water samples are sent to an accredited lab for determination of suspended sediment concentration by vacuum filtration (ASTM D3977B). In addition, site maintenance is completed, and the general condition of the road surface is noted.

The sediment tubs are emptied and measured at the end of the runoff producing season in June. Representative samples of the sediment settled in the tub are dried and analyzed at an accredited lab to determine particle density (ASTM D854) and particle size (ASTM D6913 and ASTM D7928). The monthly

suspended sediment volume is determined by multiplying the monthly tipping bucket tips by the tip calibration volume and applying the monthly average suspended sediment concentration value. The annual suspended sediment mass is the sum of the monthly masses. The sum of the monthly suspended sediment masses and the sediment tub mass can be expressed as total mass per year (kg/yr) or divided by road surface area for $kg/m^2/yr$.

In the 2019-2020 water year, ten sites produced higher-than-expected flows due to the interception of abundant shallow groundwater. These high flow sites overwhelmed the original sampling design, requiring modifications at those sites. An improved flow sampling method was prototyped and constructed in fiscal year 2021 to sample the high flow sites that behaved like small streams. A 7" V-notch weir was designed and tested to measure flow with an Onset pressure transducer system to measure the depth of flow through the weir. The flow exiting the weir passes through a flow-proportional splitter that samples approximately 20% of the discharge, with precise percentages determined for each site through a calibration each year. This flow is then passed on to the previously constructed splitter in the tipping bucket and the split volume is stored in the standard SST (Figure 1.5). The tipping bucket at these sites serves as a secondary flow measurement as well as the suspended sediment sample source to the SST.

The equipment improvements allow us to collect data on a critical portion of the road system that is intercepting and transporting large amounts of water in the roadside ditch. This is important because these roads are more likely to be routing water and sediment from their culvert discharge points overland to the nearby stream channel.

Figure 1.5 *V-notch weir and flow-proportional splitter prototype in upper photo. View from inside the tub along the water flow path in lower photo.*

1.4 Results

1.4.1 Status of Data Collection and Sites

In the first full year of the Major Experiment (2019-2020), we collected data at 76 site locations (KID-4 and KID-39 built in the following year). Annual sediment tub records were collected in all locations, but some sites experienced periodic technical problems due to higher-than-expected flows and improper site construction/equipment installation. As such, full flow and fine sediment records are available for only 31 sites in the first year (Figure 1.6 and Figure 1.7). In 2020-2021, work was completed to improve the performance of the poorly constructed/installed sites, and high-quality data was collected from all sites except the 10 high-flow sites (Figure 1.8). Gaps in the 2019-2020 flow data will be filled using the 2020-2021 flow data regressed against the suspended sediment measurements. We expect to record complete hydrographs from the 10 high flow sites in 2021-2022 after installation of the weirs.

In both water years, rainfall in the volcanic province has been nearly half of that in the siltstone province (Figure 1.9). Rainfall at the coastal siltstone sites was in the expected range of 100 inches per year, while the interior volcanic sites averaged closer to 60 inches per year. The siltstone sites on the Melbourne and Delezenne roads had intermediate rainfall values.

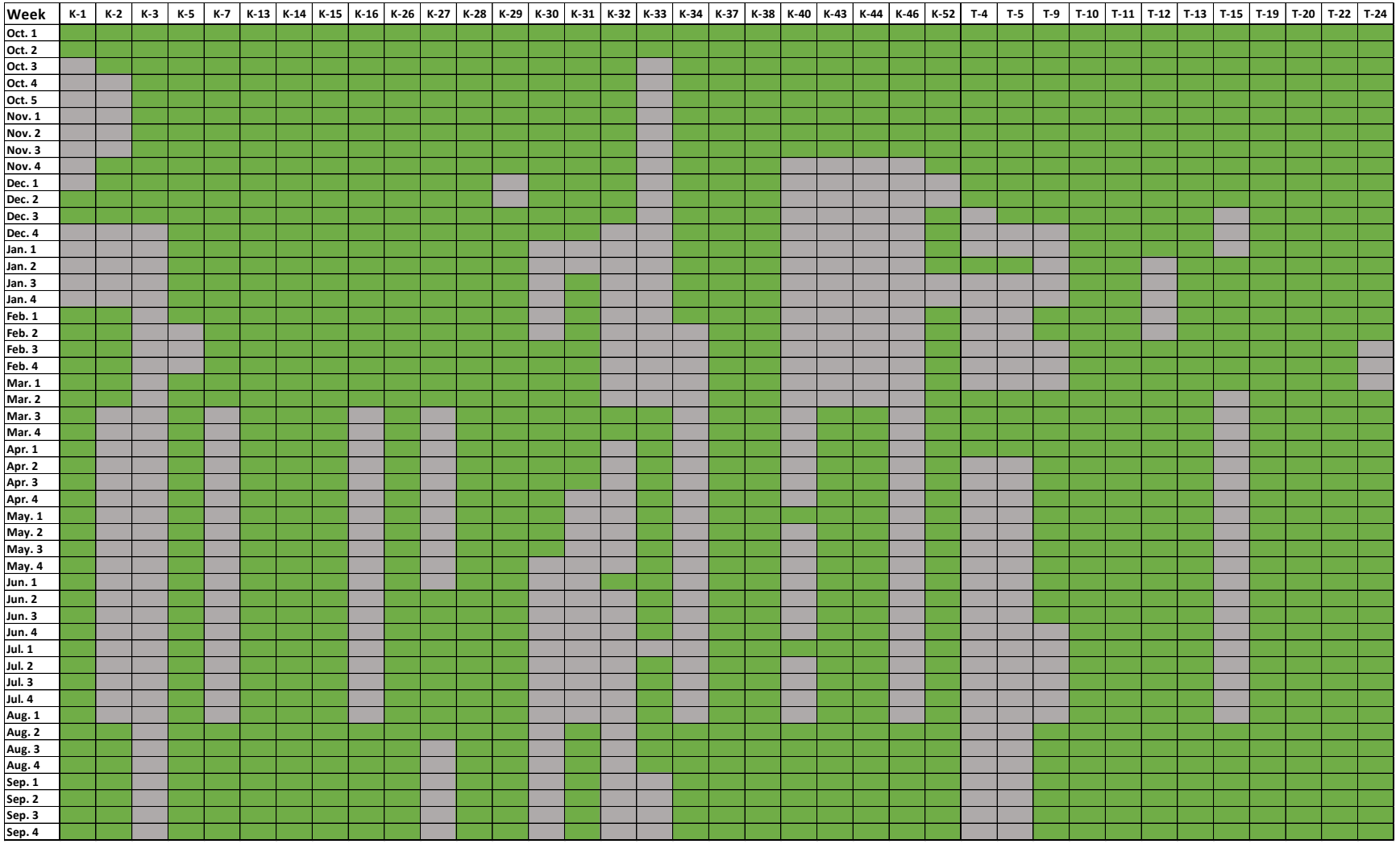

Figure 1.6 *Water year 2020 weekly flow data quality by field site in the volcanic province. Field site ID is shown on the top line. Gray boxes indicate weeks with potentially compromised field data.*

Figure 1.7 *Water year 2020 weekly flow data quality by field site in the siltstone province. Field site ID is shown on the top line. Gray boxes indicate weeks with potentially compromised field data.*

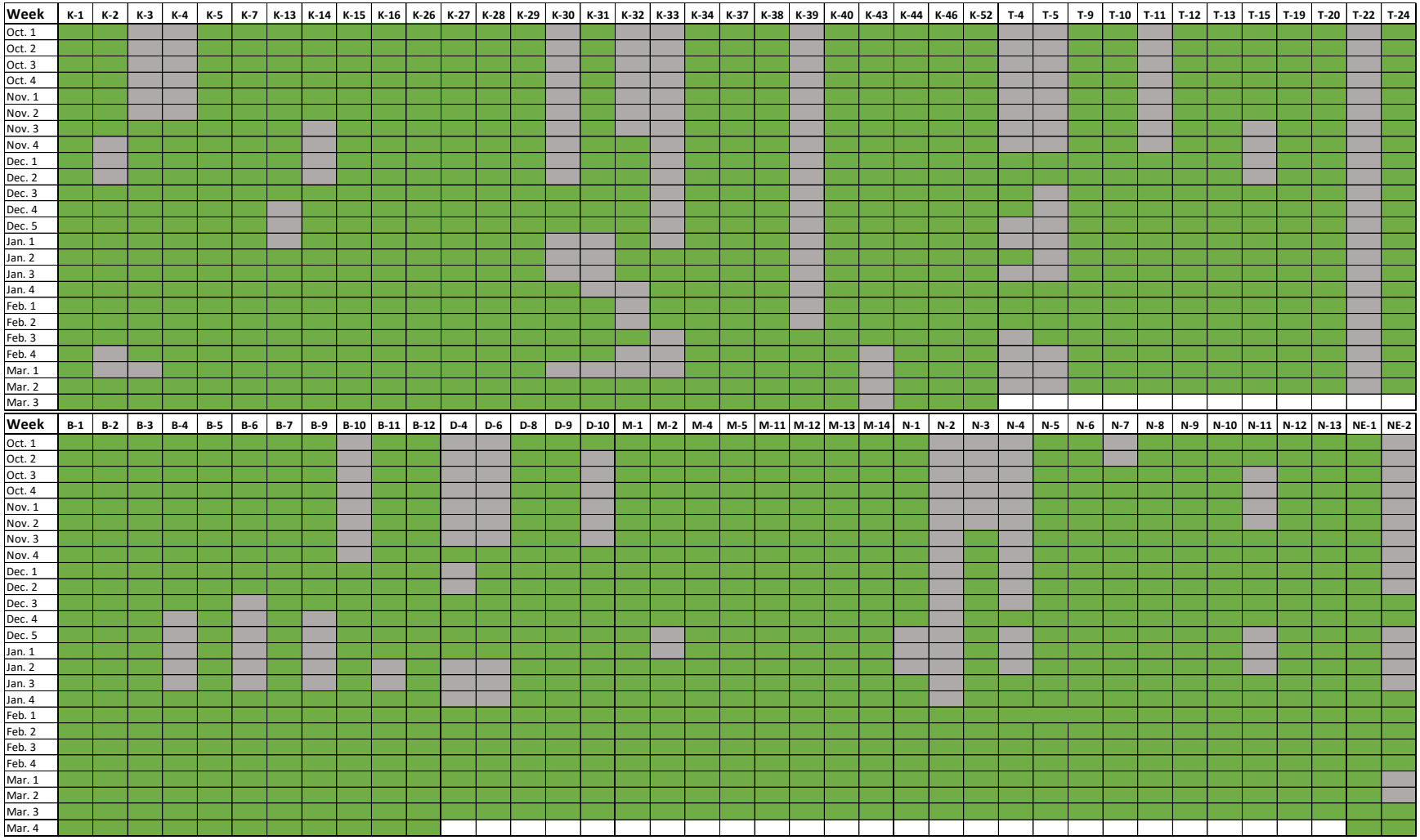

Figure 1.8 *Water year 2021 weekly flow data quality by field site. Field site ID is shown on the top line. The upper figure represents the volcanic province and the lower figure the siltstone province. Gray boxes indicate weeks with potentially compromised field data.*

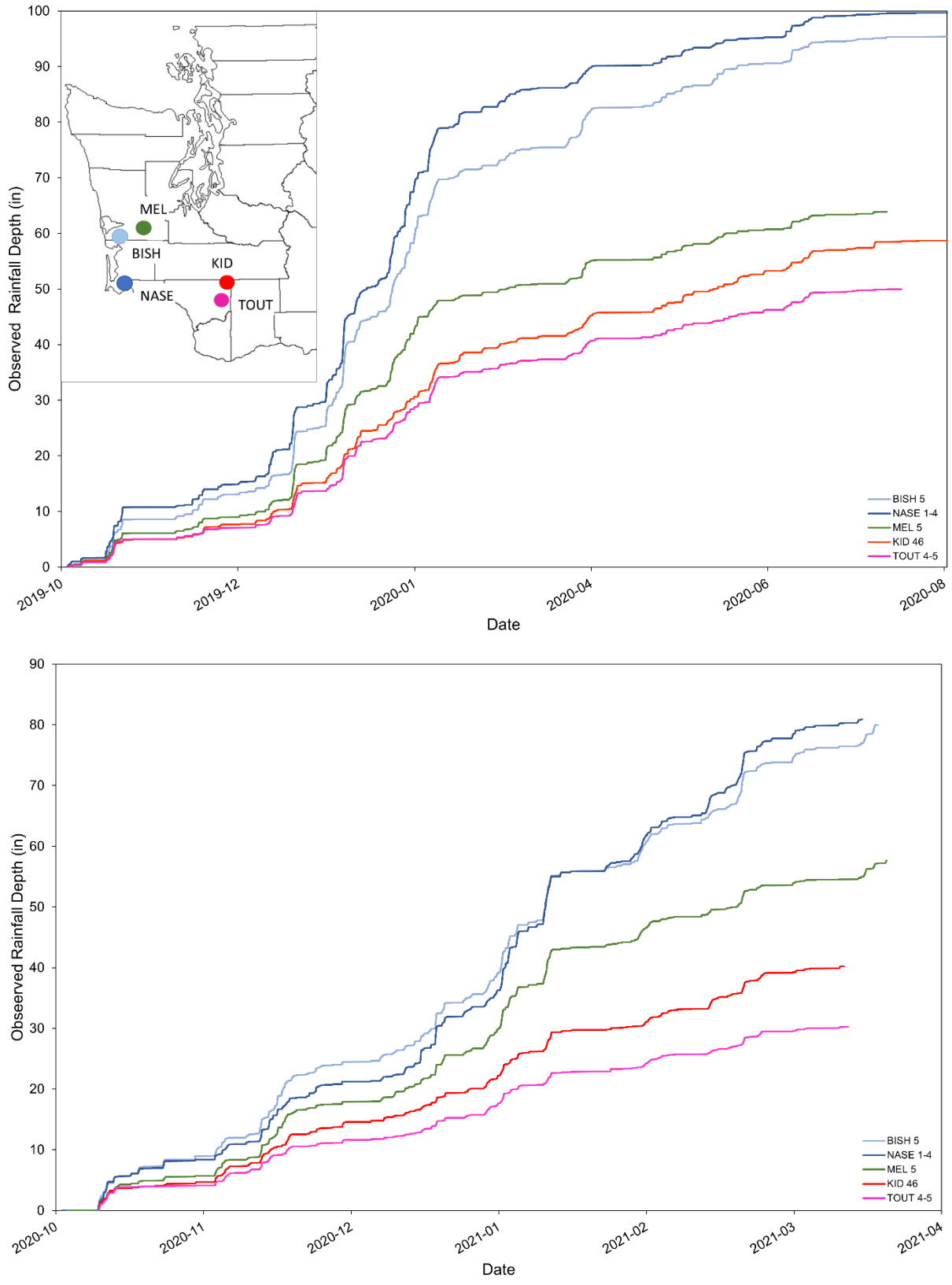

Figure 1.9 *Precipitation from representative rain gages throughout the study area for water year 2019-20 upper and 2020-21 in the lower figure.*

The hydrologic response of the sites can be grouped by the runoff response time (Figure 1.10, Figure 1.11, and Figure 1.12). Most sites appear to respond quickly to direct rainfall on the road prism as shown by KID-37 in Figure 1.10; these are likely dominated by road surface runoff. A subset of sites, such as KID-29 shown in Figure 1.10, exhibited a much longer response time following rainfall initiation and these sites typically produce substantially more water.

Figure 1.11 compares a site with a quick response (KID-37) and a site with a slower response (KID-34) on the same plot for water year 2021. Similar to KID-29 (Figure 1.10), KID-34 (Figure 1.11) has a longer response time (longer tail end on the hydrograph), meaning that sites like these are likely receiving substantial water from cutslope interception. These slow response time roads have the potential to transport sediment from the road to the stream for a longer period than roads with a faster hydrologic response time.

In addition to displaying different hydrologic responses, sites in a small geographic area with equivalent rainfall can have very different total water volumes (Figure 1.12). Future analyses will investigate the influence of site-specific variables, such as watershed characteristics, that may explain the observed variability.

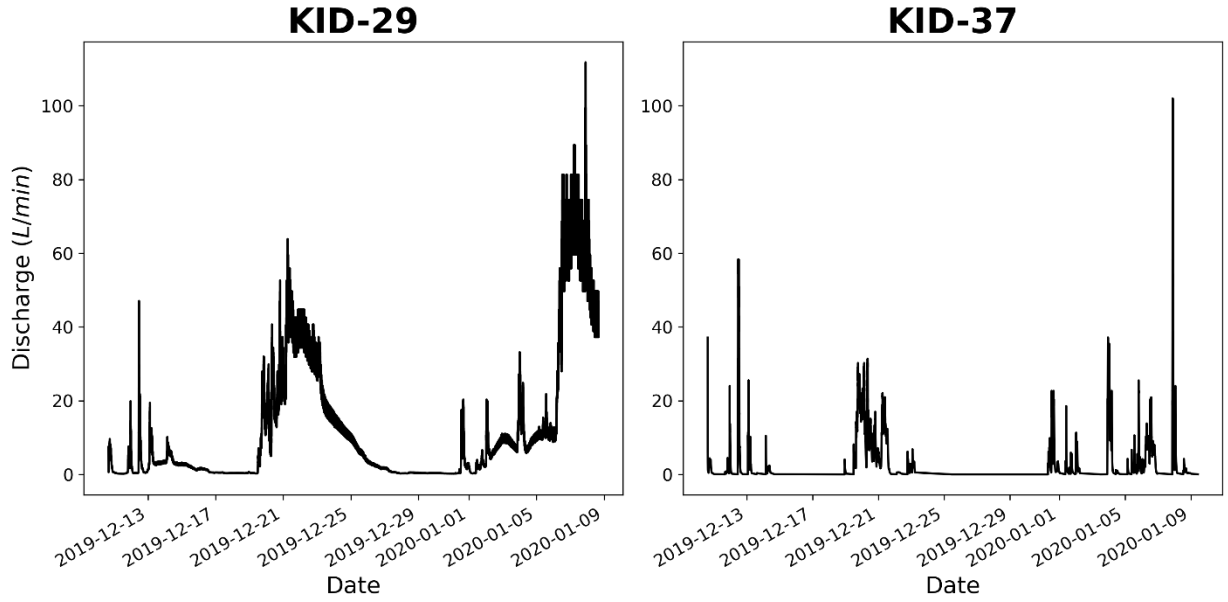

Figure 1.10 *Examples of relationships between rainfall and slow runoff at Kid-29 and fast runoff at Kid-37 for the 2020 water year.*

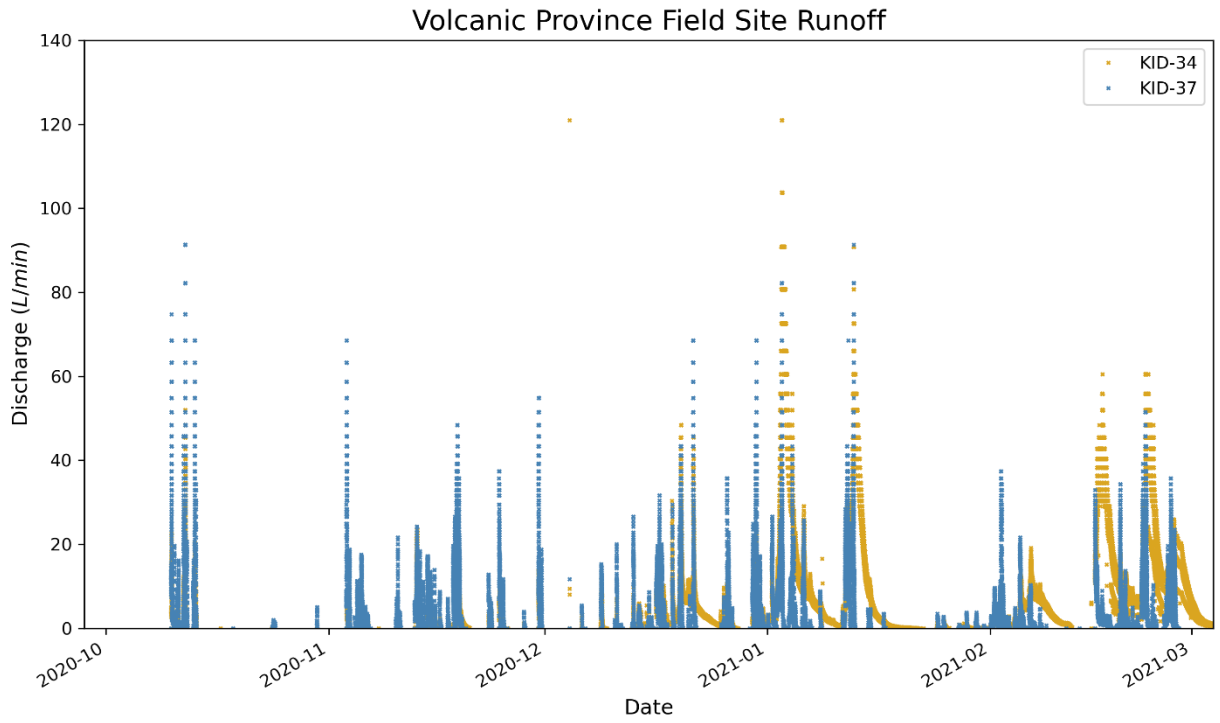

Figure 1.11 *Examples of a site hydrographs for the 2021 water year for the volcanic province.*

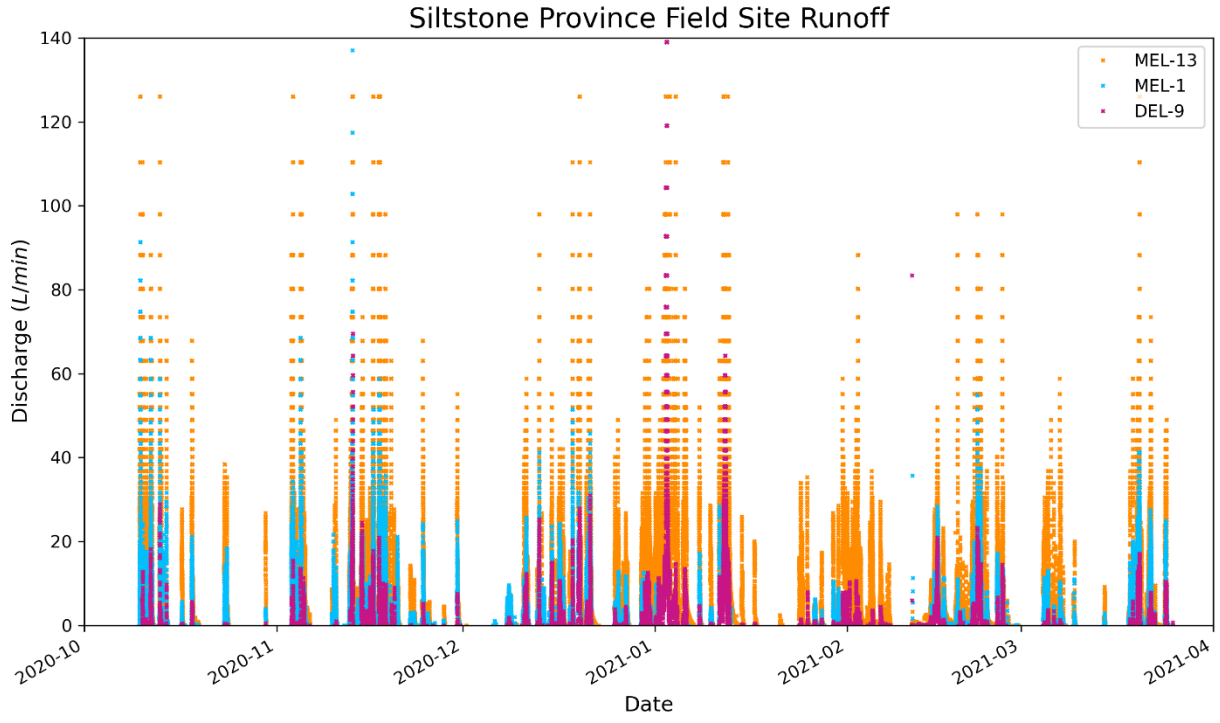

Figure 1.12 *Examples of site hydrographs for the 2021 water year for the siltstone province.*

1.4.2 Analysis of Sediment Data from the 31 Sites with Full Data from 2019-2020

The 31 sites with complete data offer some insights that support the aims of the study and provide feedback to help identify sensitivities in the data collection procedures. In the preliminary analysis, we look at sediment trap efficiency and controls on site sediment yields. Summary sediment, flow, and site information are provided in Table 1.2.

Table 1.2 *Sediment, flow, and site characteristic data for the 31 sites with complete data for 2019-2020.*

Site	Suspended Sediment (kg)	Tub Sediment (kg)	Total Sediment (kg)	Flow (m^3)	Geology	Road Slope	Rock Quality (good, marginal)	Ditch veg.	Traffic
TOUT-10	6.2	41.06	47.27	29.62	V	3%	g	grass	H
TOUT-11	9.1	5.80	14.95	74.94	V	3%	g	grass	H
TOUT-13	0.0	3.74	3.77	2.77	V	5%	g	grass	H
TOUT-15	3.7	13.81	17.51	28.19	V	4%	m	grass	H
KID-7	6.2	31.23	37.45	39.99	V	8%	g	grass	M
KID-13	22.7	13.72	36.42	958.00	V	6%	g	grass	L
KID-14	114.8	24.73	139.57	713.98	V	5%	g	grass	L
KID-15	53.1	13.30	66.37	637.78	V	5%	g	grass	L
KID-16	33.1	2.83	35.97	996.68	V	5%	g	grass	L
KID-26	159.7	46.46	206.21	703.24	V	4%	g	grass	H
KID-28	100.7	27.37	128.05	534.85	V	3%	m	grass	H
KID-37	90.6	15.87	106.51	336.62	V	4%	g	grass	L
DELE-6	28.1	12.40	40.48	578.79	S	7%	g	grass	M
DELE-8	71.9	20.67	92.56	664.36	S	3%	g	grass	M
DELE-10	86.3	161.71	247.98	308.71	S	6%	g	grass	M
MEL-2	469.5	670.19	1139.72	799.41	S	10%	g	bare	H
MEL-4	68.9	251.51	320.41	248.91	S	7%	g	grass	H
MEL-5	317.3	258.02	575.31	617.59	S	7%	g	bare	H
MEL-11	4.1	4.48	8.61	368.13	S	4%	g	grass	M
MEL-12	26.4	12.94	39.32	428.84	S	5%	g	grass	M
MEL-14	140.2	187.52	327.67	459.87	S	10%	g	grass	M
BISH-2	49.5	22.99	72.49	946.91	S	2%	m	grass	M
BISH-3	26.3	35.29	61.63	328.64	S	3%	m	grass	M
BISH-4	11.7	1.29	12.94	1111.69	S	13%	g	grass	L
BISH-6	23.6	31.40	55.04	758.74	S	11%	g	grass	L
BISH-7	11.5	4.35	15.85	223.53	S	12%	g	grass	L
BISH-11	7.1	2.99	10.04	1044.99	S	5%	g	grass	L
NEWS-19	1.6	0.71	2.26	335.05	S	4%	m	grass	M
NEWS-20	5.6	9.34	14.95	691.23	S	5%	g	grass	M
NASE-10	14.8	18.55	33.39	104.70	S	13%	m	grass	L
NASE-11	6.1	26.47	32.52	112.76	S	13%	g	grass	L

Total sediment yield from 2019-2020 for the 31 sites fits into a conceptual model framed in terms of limitations in sediment availability and capacity to transport sediment. Broadly, high traffic sites have greater sediment availability, and their transport capacity can be framed in terms of a stream power concept. Classically, stream power uses peak flow rate, but in Figure 1.13, the transport capacity is framed as total annual flow multiplied by slope, acknowledging the correlation between annual flow and peak flow rates. Given non-linearities in transport capacity as a function of flow rate, other formulations to estimate transport capacity will be considered. In Figure 1.13, the limitation by flow energy is seen as a dependence in flow x slope only for sites having high or moderate traffic levels (e.g., those without a sediment availability limitation). This dependency is shown with the red dashed line, which is a fit for the high traffic sites. Note that this is similar to the regression used in Luce and Black (1999), which examined freshly disturbed sites with substantial amounts of readily available sediment and found a dependence on site length—a rough proxy for flow—and slope. For sites where sediment production is limited relative to the capacity to transport it (i.e., those with low traffic) there is no dependence on flow x slope. Moderate traffic sites fit across this range of behaviors, and it is possible that the total amount of traffic may be inadequate to frame the sediment availability because such availability may also depend on timing of traffic.

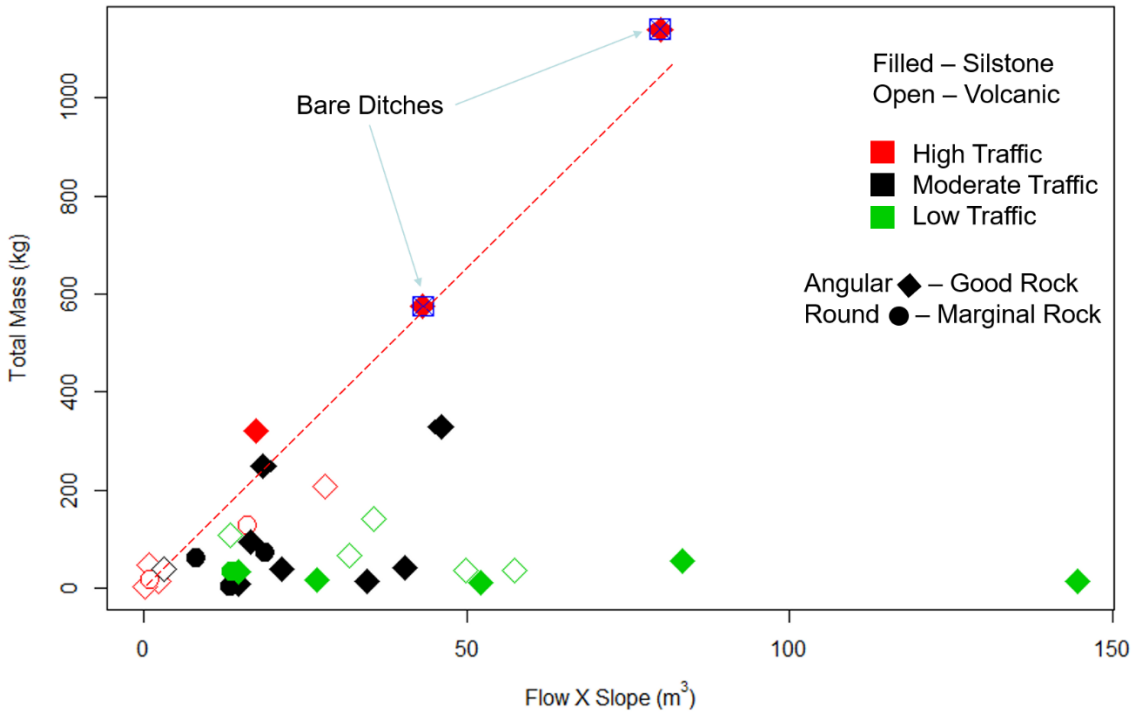

Figure 1.13 *Site total sediment yield as a function of total flow "energy" for 2019-2020.*

The analysis with 31 sites has limitations beyond uncertainty in details about the best metrics to use. Very limited data with both high traffic and high flow x slope exist, and the two sites with those characteristics also have ditch lines with limited grass cover compared to most of the other sites (Figure 1.13). The limited grass cover is partially the result of tight corners where some vehicles track in the ditch line. This would confound the effects of traffic and ditch treatment if we were trying to isolate the effects of those BMP from this single year of data. Additionally, the lowest flow sites are dominated by high traffic observations and, ideally, there would be some representation of sites with less disturbance. However, it was most critical to have had high traffic samples combined with low flow because these observations demonstrate that either low flow OR low traffic yield low sediment yield, and that high sediment yield requires both high flow AND high traffic. Because traffic levels for the sites vary over time, additional insights may be gained when sites with a given flow level see variations in traffic over time. Additionally, the Short-Time-Scale Interactions experiment will help inform the detailed processes driven by traffic. As data from more sites become available, we should be able to evaluate the "limitation model" more robustly to contextualize multiple BMP.

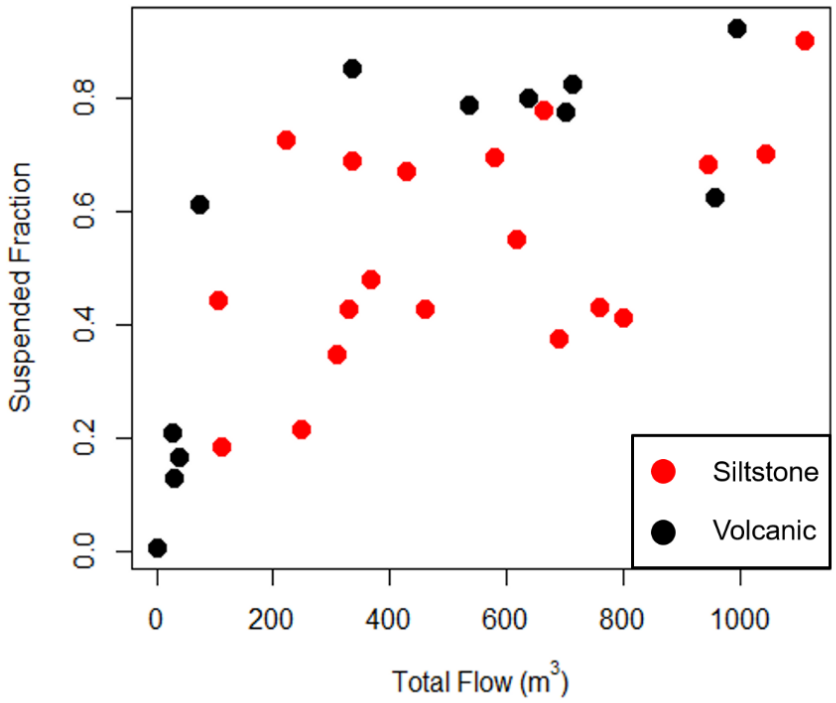

Figure 1.14 *Suspended sediment fraction passing through sediment traps (tubs) as a function of the total flow volume for 2019-2020.*

One of the research questions we are examining is the potential benefit of using sediment traps in the ditch as a BMP. Sediment traps are typically constructed as a small settling pond in the roadside ditch. One question concerns how much sediment such a trap might retain given the flow and size of the depression (trap efficiency). Sediment trap efficiency was examined as a function of the total flow through the tub over the year and underlying geology (Figure 1.14). Broadly, sediment trap efficiency is constrained by flow such that very high trapping efficiency (low suspended fraction) can be obtained only when flow is low. Low trap efficiency was also obtained from sites with relatively low flow (Figure 1.14). At volcanic sites, high efficiencies at the lowest flows transitioned rapidly to low efficiencies at still fairly low flows, and low efficiencies were seen at the majority of flow levels. In contrast, there was substantial variability at siltstone sites even for a given flow rate. We will continue to evaluate these data and new incoming data to consider 1) effects of particle size distributions of sediment flowing to the tank, and 2) effects of other flow metrics (e.g., peak flow rate or a high quantile flow rate). In Figure 1.14 we use total flow, which correlates with peak flow rates. However, if most sediment entrainment occurs at high flow rates and if high flow rates could resuspend sediment deposited during lower flows, high flow rates may be a better context to evaluate efficiency that we can explore in the future. We also have sediment particle size distributions of what was retained in the tanks, which may offer an opportunity to evaluate what size fractions are retained by the sediment traps as a function of flow.

Flow and suspended sediment data show that a large fraction of the total sediment can pass through the sediment tubs. This knowledge informs our understanding of sediment trap efficiency and will be informative for the Sediment Trap Efficiency parameterization experiment. This parameterization experiment is intended to characterize the effectiveness of in-ditch sediment traps that are much smaller than the sediment tubs used in the Major Experiment. The current data serve as an “optimistic” end-member sample of the potential effectiveness of sediment traps.

2 Continuing Model Development

We have hypothesized and developed a preliminary, spatially lumped, forest road sediment balance model that demonstrates the flow of sediment from a representative road segment and the vertical sediment exchange among conceptual layers. The domain of the topic spatially lumped model is an 80-meter by 9-meter segment of road that is divided into 1-meter by 4.5-meter sections (Figure 2.1). Every meter-long section is assumed to have the same characteristics such that sediment production in one section can be extrapolated to every other section and summed to obtain the total sediment yield.

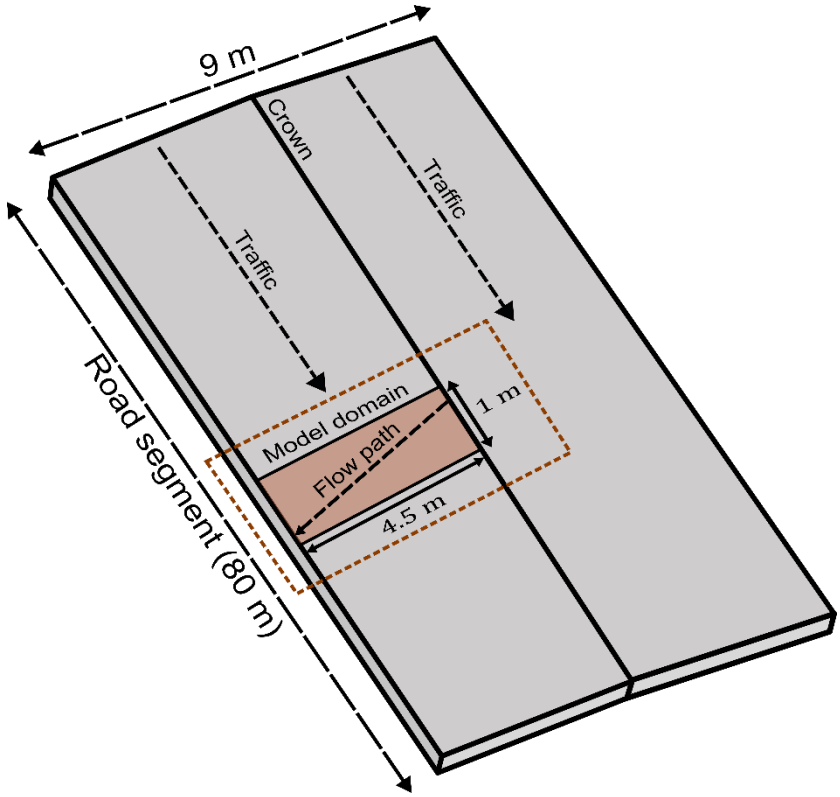

Figure 2.1 *Schematic of modeling domain.*

A tri-layered conceptualization with five main fluxes (two inter-layer pumping fluxes, two intra-layer crushing fluxes, and one lateral transport flux) acting on the system is used to model the physical processes to ensure conservation of mass. Each modeled road cross section is divided into three main layers, from top to bottom: the transport-available fines (TAF) layer, S_f; the road surfacing layer, S_s; and the ballast layer, S_b (Figure 2.2). S_s and S_b are further divided into fine and coarse fractions of material such that:

$$S_s = S_{sf} + S_{sc} \quad (1)$$

$$S_b = S_{bf} + S_{bc} \quad (2)$$

where the *f* subscript denotes the fine fraction of material, and the *c* subscript denotes the coarse fraction of material. Currently in the model, these sediment size fractions are grouped into buckets of “small enough to transport” and “too big to transport” to simplify parameters.

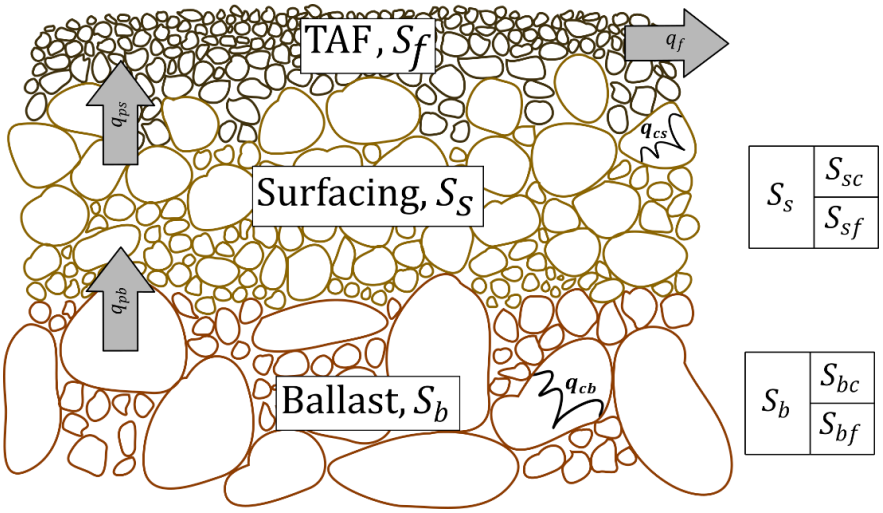

Figure 2.2 *Tri-layered conceptualization.*

The conceptual TAF storage layer is the uppermost road layer that contains only fine material available for water-driven transport. This layer can be likened to an "active layer" of a riverbed (e.g., Hirano, 1971). The TAF layer connects the road domain with the domain outside the road prism and is the layer in which sediment transport occurs. The two main fluxes acting on this layer are the TAF lateral transport flux, q_f, and the vertical surfacing pumping flux, q_{ps}. q_f describes the fine sediment leaving the road prism and is governed by a common sediment transport equation. q_{ps} is an inter-layer transportive flux that describes the pumping of fine sediment from the surfacing layer, S_{sf}, into the TAF layer, S_f (Figure 2.3).

The surfacing storage layer is the middle layer of the cross-section and is typically a mixture of approximately 80% gravel and 20% finer material that is between six and twelve inches deep (e.g., Figure 5.5). This layer couples to both the TAF and the ballast and is the most active layer in terms of the number of fluxes acting on and within it. The three fluxes acting on this layer are the surfacing pumping flux, q_{ps}; the surfacing crushing flux, q_{cs}; and the ballast pumping flux, q_{pb}. As described above, q_{ps} is an inter-layer transportive flux that describes the pumping of fine sediment from the surfacing layer, S_{sf}, into the TAF layer, S_f. q_{cs} is an intra-layer generative flux that describes the crushing of coarse surfacing material, S_{sc}, into fine surfacing material, S_{sf} (Figure 2.4). q_{pb} is an inter-layer transportive flux that describes the pumping of fine sediment from the ballast layer, S_{bf}, into the fine sediment of the surfacing layer, S_{sf}.

The ballast storage layer is the lowest layer of this conceptualization and is typically larger material with interstitial space occupied by a fine material matrix. The ballast transitions to native material as you move farther down the stratigraphic column, but the native material is not considered in this analysis. This layer couples to the surfacing via one of two fluxes. The two fluxes acting on this layer are the ballast crushing flux, q_{cs}, and the ballast pumping flux, q_{pb}. q_{cb} is an intra-layer generative flux that describes the crushing of coarse ballast material, S_{bc}, into fine ballast material, S_{bf}. q_{pb} is an inter-layer transportive flux that describes the pumping of fine sediment from the ballast layer, S_{bf}, into the fine sediment of the surfacing layer, S_{sf}.

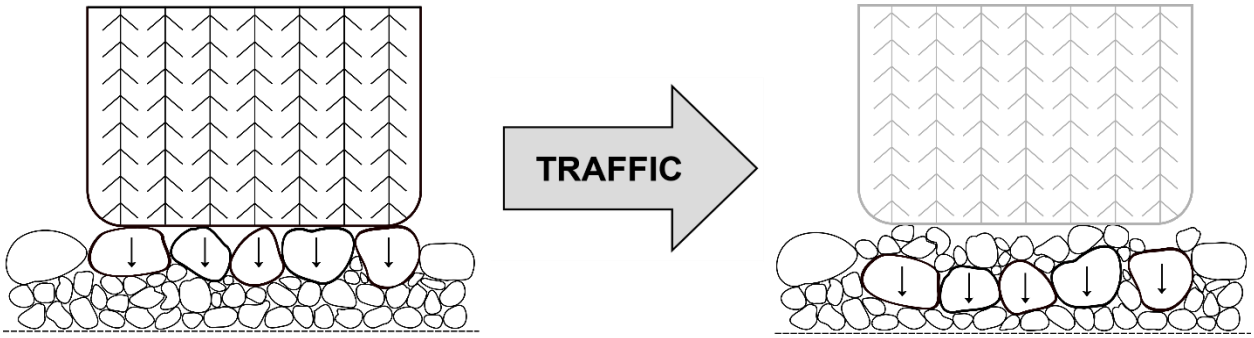

Figure 2.3 *Schematic of the pumping process. Larger sediment is layered over finer sediment (left) and when traffic is applied (center) the larger sediment gets pushed down which forces the finer sediment upwards (right). Image not to scale.*

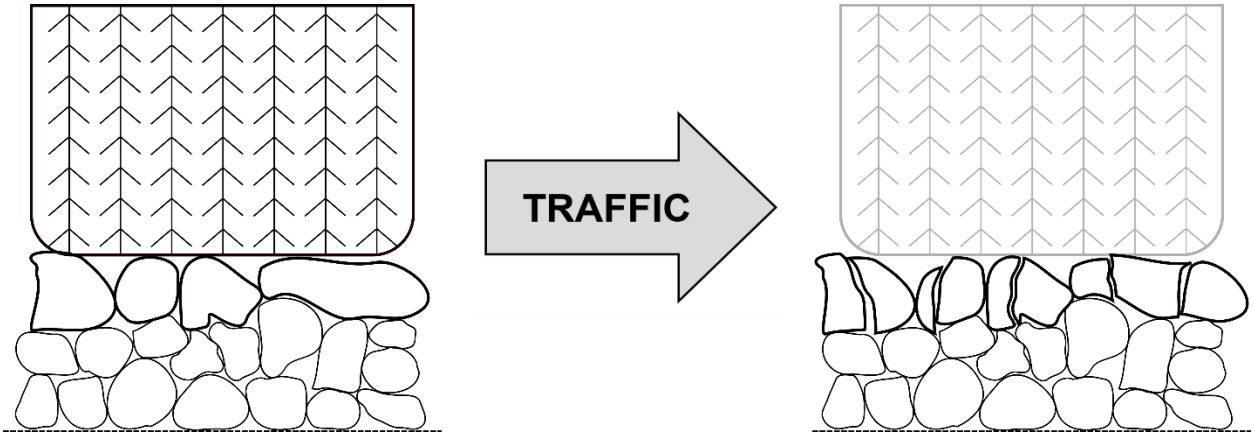

Figure 2.4 *Schematic of the crushing process. On a typical road surface aggregate (left) when traffic is applied (center) the larger sediment breaks down into finer sediment (right). Image not to scale.*

The pumping and crushing fluxes—q_{ps}, q_{pb}, q_{cs}, and q_{cb}—are modeled via equations we developed based on hypotheses developed from literature and field observations (e.g., Reid & Dunne, 1984; Ziegler et al., 2001a; Foltz & Truebe, 2003; Rhee et al., 2018), while the transport flux is modeled by Govers' equation for shallow overland flow (Govers, 1992). The transport flux also includes a shear stress partitioning component that changes based on how "full" the TAF layer is. If the fine sediment of the TAF layer only fills some of the voids between larger sediment in the surfacing, the shear stress available to transport the sediment will be less because the larger sediment acts as an "obstruction". These processes, plus a simple stochastic model representing truck passes are the basis of the spatially lumped model. Each layer is a depth of storage because the value has been normalized by the length (1 m) and width (4.5 m) of road.

Below are preliminary results from an example model run forced using rainfall data from a gage at Elk Rock near Mount St. Helens (MesoWest, 2020). In the plot of fine sediment storage (Figure 2.5), the layer has been initialized at "full" TAF depth—a condition that corresponds to a road that has had many truck passes and no rainfall—such that the model does not require a spin-up period (i.e., time to fill up the TAF layer to produce any sediment transport). A large storm occurs at the beginning of the period which flushes a lot of the fine sediment away—this is also called the "first flush" phenomenon (van Meerveld et al., 2014). The ups and downs of the fine sediment storage are due to traffic running over the road surface, causing a disturbance (increase), and then rainfall occurring, washing the fine sediment away (decrease).

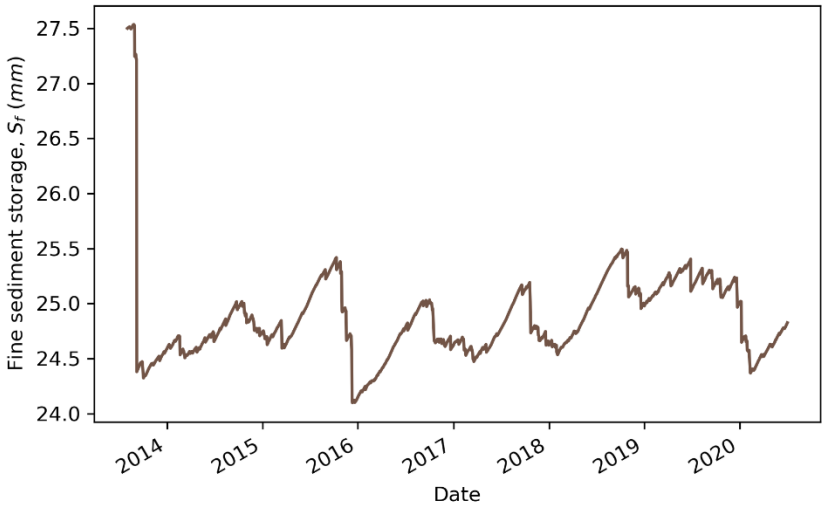

Figure 2.5 *Fine sediment storage depth in the TAF over time. The TAF layer was initialized at 27.5 mm to avoid a model spin-up period.*

The next figure (Figure 2.6) demonstrates the use of shear stress partitioning when modeling sediment transport. The dark green line represents the reference transport capacity, or what depth of sediment would be transported per storm had the shear stress not been partitioned. The golden line shows the actual depth of sediment transported per storm—these values are a lot lower than the reference transport capacity because of shear stress partitioning.

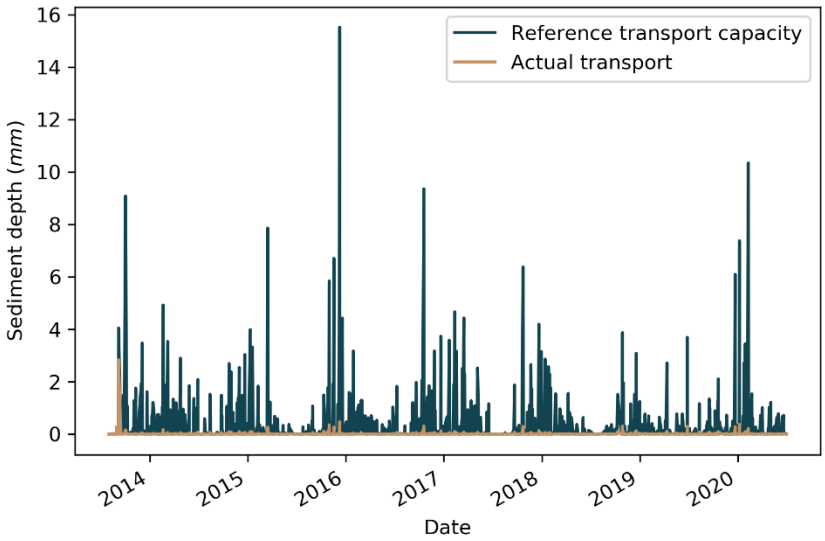

Figure 2.6 *Reference transport capacity depth vs. actual transport depth over time.*

The final plot (Figure 2.7) shows the annual sediment load per meter of road. In the first year, the first flush phenomenon is readily apparent. The overall values of mass per meter of road are high compared to our collected data (see Figure 1.13), which is likely due to our current parameter estimations and the fact that this spatially lumped model includes only the road prism currently. This model will be further developed in the coming biennium.

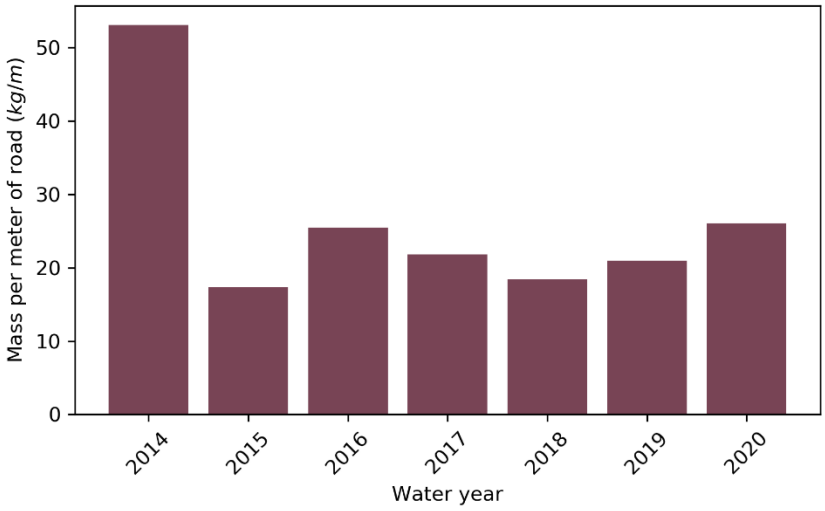

Figure 2.7 *Sediment load per meter of road for each water year of the model run.*

3 Data Analysis Related to Model Development

Much of the data collected so far—total sediment, flow discharge, traffic counts—are not currently applicable to the spatially lumped model due to model scale limitations. However, these data will be crucial for model calibration and validation once the model includes accurate estimates of parameters related to the Short-Time-Scale Interactions and the Ditch Line Hydraulics experiments. The required parameter estimations will be incorporated in the coming biennium as the previously mentioned parameterization experiments are carried out.

In March 2021, a small-scale test for the Short-Time-Scale Interactions experiment (Section 5) was conducted to test and refine methods. This pilot showed measurable differences between before and after traffic runoff. However, data from the full Short-Time-Scale experiment is needed to incorporate into the model, and as such, further data analysis related to model development has yet to be carried out in full.

4 Sediment Trap Efficiency Experiment—Delayed

The Sediment Trap Efficiency Parameterization experiment was delayed due to COVID-19. The results from analysis of the Major Experiment's sediment tubs (Section 1.4.2) may provide enough information that this parameterization experiment may not be necessary. Specific tests could help in further understanding or extrapolating the tub/trap efficiency data with respect to application of sediment traps in an operational context (e.g., for smaller traps) and therefore make the Sediment Trap Efficiency parameterization experiment unnecessary. The utility of completing the Sediment Trap Efficiency parameterization experiment will be determined later.

5 Short-Time-Scale Interactions Experiment

To better understand how to efficiently control roads as a sediment source, we need to study the contribution of fine sediment on short-time scales in the context of overall annual site sediment production. The focus of this experiment is to measure sediment detached and transported from the road tread under variable surfacing rock quality, truck frequency, and rainfall intensity. This experiment will determine how much sediment is produced from the road surface and the fate of that sediment during a rain event after a truck pass.

Due to COVID-19 work and travel restrictions, we were not able to conduct the full Short-Time-Scale Interactions parameterization experiment in this biennium. However, field equipment and methods were tested during a pilot test of the field methodology on March 1-3, 2021.

Figure 5.1 *New fine sediment pumped from the roadbed by the passage of a loaded log truck.*

The Short-Time-Scale Interactions experiments will examine the within-site contribution of sediment from traffic relative to that from ditch and cutslope by sampling water from: a) specific locations on the road tread b) segments of the road tread as it enters the ditch from the roadside; c) the ditch upstream of the tread contribution; and d) the outlet of the cross-drain culvert after the first two have combined. In the pilot experiments, we tested methods for isolating specific road elements for sediment sampling (a and b above) and tested the sampling equipment to removing fine sediment from the road surface (Figure 5.2). An example of fine sediment runoff from the road surface is shown in Figure 5.3.

Figure 5.2 *The fine sediment that is available for transport on the road surface due to recent traffic is carefully washed from the isolated sampling area and evacuated into a sample container for sediment analysis.*

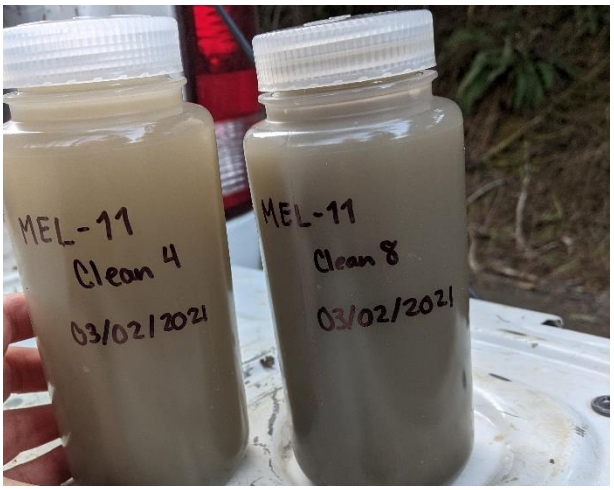

Figure 5.3 *Wash-off samples collected before (Clean 4) and after (Clean 8) multiple pickup truck passes over a 1'x1' area. The change in clarity of the samples demonstrates an increase in fine sediment post truck pass.*

Methodology was tested using repeated high-resolution photography to document the changes in the textural composition of the road surface following the passage of heavy vehicles (Figure 5.4 and Figure 5.5). We collected a library of images to test the image processing software that will be used to measure the changes in particle sizes on the road surface.

Figure 5.4 *A comparison of a road surface with abundant fine sediment on the gravel on the left image. On the right is an adjoining road segment surface that was washed clean of the fine sediment to expose the gravel.*

Figure 5.5 *A comparison of the armoring of the surface (circled in pink) in contrast to the abundant fine material in the subsurface (circled in blue).*

6 Ditch Line Hydraulics Experiment

The objective of the Ditch Line Hydraulics (DLH) parameterization experiment is to determine the effects of three roughness-varying ditch line BMP on the hydraulics of ditch lines running alongside mainline logging roads. Understanding the hydraulics of these ditch lines will allow us to further understand: 1) the total shear stress acting on the "bed" of the ditch; 2) the shear stress acting on the sediment grains; and 3) the effects these BMP have on the erosion and sediment transport of the ditch.

Through measurement of various hydraulic and sediment parameters, we will be able to partition shear stress such that we can examine the relationship between the grain shear stress and sediment yield. We will also be able to run our conceptual model of sediment production at the scale of the ditch line for the same duration as this parameterization experiment to obtain sediment yield predictions. These predictions, as well as the sediment size distribution used in the model, will be compared with properties of the sediment collected in the sediment tub. Such analysis will quantify the efficacy and efficiency of the roughness-varying ditch line BMP being used at each site, as well as further develop and validate our model.

The first year of the DLH parameterization experiment was carried out in May 2021. Over the course of five days, the field team carried out seven different experimental runs: KID-14 Bare, KID-15 Grassed, KID-14 Wattles, KID-39 Gravel, MEL-12 Grassed, MEL-13 Bare, and MEL-13 Wattles. Section 6.1 describes the methodology used in the field. Section 6.2 goes through the equations used to calculate shear stress, drag coefficients, and Manning's roughness. Section 6.3 provides preliminary results from data analysis and are subject to change based on further discussion within the project team.

6.1 Methods

1. Measure the slope of the lower half of the ditch line (lowest 40 meters).
    a. Place a measuring tape in the ditch line.
    b. Measure elevation with a rod and level every 4 meters.
2. Measure the dimensions of five sample cross sections in the 40-meter segment.
    a. Set meter-long level across the ditch.
    b. Measure the elevation drop every 10 cm.
3. Sample about 1/2 kg of soil from near the surface at each cross section and place each sample into a soil bag.
4. Take photographs of the ditch line pre-experiment at each of the five cross sections.
5. **For grassed sites only:** Collect 10 samples of grass from the upper 40 meters of ditch line.
    a. Put down quadrat (30cm x 30cm square) in a randomly determined location.
    b. Take photograph from above.
    c. Clip all grass within the quadrat using grass shears and place the sample in a bag for later drying and weighing.
6. **For wattle sites only:** Place and stake wattles.
    a. The number of wattles placed in the ditch line varies at each site depending on the ditch line elevation profile. The bottom of one wattle is placed at the same elevation as the top of the next lower wattle.
7. Run a slow rate of water down ditch line for approximately 15 minutes before experimental runs to wet the soil.
    a. Place sieve and bucket below culvert.
    b. Set turbidimeter in the bucket and start recording.
    c. Set conductivity sensors (salt probes) in ditch at 4 m and 36 m and start recording.
8. Turn water to initial flow rate (approx. 15 gpm), and let it stabilize.
    a. Read and record the flow meter value and time and begin the stopwatch.
        i. Read and record the flow meter value every minute on the minute for the duration of the experiment.
    b. Clean conductivity sensors.
    c. Introduce salt tracer at the top of the experimental site and monitor the values at each of the conductivity sensors.
    d. Read and record initial salt concentration values.
    e. Take grab samples from bucket holding turbidimeter.

   f. Place flags at high water marks at each cross section.
   g. When the salt concentration at the lower sensor returns to its initial value:
      i. Read and record the flow meter value and time and stop the stopwatch.
      ii. Collect sediment from sieve and place into bag.
   h. Replace sieve.
   i. Siphon tank to reduce water level.
9. Increase flow rate (approx. 25 gpm), and let it stabilize.
   a. Repeat steps 8a-i.
10. Increase flow rate (approx. 40 gpm), and let it stabilize.
   a. Repeat steps 8a-i.
11. Calibrate conductivity of salt probes for three minutes.
12. Stop recording salt concentration and turbidity.
13. Turn off water.
14. Measure flow widths for each of the experimental runs at each of the cross sections.
15. Take photographs of ditch line post-experiment.
16. Sample about 1/2 kg of soil from near the surface at each cross section and place each sample into a soil bag.
17. Carry out analysis:
   a. Calculate hydraulic radii, cross-sectional areas, flows, shear stresses, drag coefficients, and Manning's roughness coefficients.

6.2 Analysis

Shear stress is the driver of sediment transport. The total shear stress acting on the ditch line is a function of the hydraulic radius of flowing water. Our controlled experiment in which the hydraulic radius could be back calculated through measurements will help us look further into the component of shear stress causing sediment to be transported (grain shear stress). Understanding the underlying mechanisms of such sediment transport will allow us to better determine which BMP will be the most effective at mitigating erosion of the ditch line and, thus, sedimentation to nearby streams.

Einstein and Barbarossa (1952) proposed to partition shear stress into various components such as the shear stress that acts upon sediment grains and the shear stress that acts upon forms in the channel (e.g., bed forms and vegetation).

$$\tau_0 = \rho_w g R S \quad (1)$$

$$\tau_0 = \tau_g + \tau_a \quad (2)$$

where τ_g is the grain shear stress and τ_a is the additional shear stress, ρ_w is the density of water, g is the acceleration due to gravity, R is the hydraulic radius, and S is the sine of the channel slope.

Using this framing, we developed and carried out the DLH parameterization experiment to look at shear stress partitioning in a roadside ditch line. In the field, we collected flow velocity data using a salt tracer as we input flow to the ditch line. We back calculated the average cross-sectional area of flow using:

$$A_f = \frac{Q}{U} \quad (3)$$

where A_f is the cross-sectional area of flow, Q is the measured flow discharge being input to the ditch line, and U is the measured velocity. In our analyses, we calculated A_f—and thus the hydraulic radius, R—using the field-measured velocity, U, and two field-measured discharge values, Q_1 and Q_{obs}, which are discharge values based on the salt tracer data and the measured outflow at the water truck, respectively.

We then calculated the hydraulic radius from:

$$R = C_{shape} A_f^{1/2} \quad (4)$$

where C_{shape} is a shape constant. Istanbulluoglu et al. (2003) present three formulations for C_{shape}— for trapezoidal, triangular, and parabolic channels, respectively:

$$C_{trap} = \frac{(z_1 - z_2)^{0.5}}{(z_1 - 2z_2) + 2({z_2}^2 + 1)^{0.5}} \tag{5}$$

$$C_{tri} = \frac{{z_2}^{0.5}}{2({z_2}^2 + 1)^{0.5}} \tag{6}$$

$$C_{par} = \frac{\sqrt{1.5}{z_1}^{1.5}}{1.5z_1^2 + 4} \tag{7}$$

where z_1 is the width-to-depth ratio and z_2 is the side slope ratio. For the sites in this study, we fitted a parabolic shape to each of the ditches based on cross-section dimension measurements (Equation 7). The values for z_1 were estimated based on measurements taken in the field during the experiment.

6.2.1 Drag Coefficients for Sediment Grains

In the case of the bare ditch line, we combined Equations (1) and (2) to get:

$$\tau_0 = \tau_g + \cancel{\tau_a}$$
$$\Rightarrow \rho_w g R S = \tau_g \tag{8}$$

As such, the bare ditch experimental run gave us an estimate of the effective shear stress available for sediment transport. This experimental run also gave us information that will aid in further experimental runs and analysis. We got an estimate of the drag coefficient for the bed, and thus the sediment grains, by writing Equation (3) as a force balance (such as in Manga and Kirchner (2000)):

$$\rho_w g R S = \tau_g$$
$$\Rightarrow \rho_w g R S = \rho_w C_B U^2$$
$$\Rightarrow C_B = \frac{gRS}{U^2} \tag{9}$$

where C_B is the drag coefficient on the bed and U is the flow velocity. Because g is a known constant and R, S, and U were measured in the field, we were able to obtain a value for C_B. C_B should remain constant even with the addition of any roughness elements. This allowed us to determine the approximate effect of different roughness elements on the shear stress.

6.2.2 Drag Coefficients for Additional Roughness Elements

After adding in roughness elements, we combined Equations (1) and (2) to get:

$$\tau_0 = \tau_g + \tau_a$$
$$\Rightarrow \rho_w g R S = \tau_g + \tau_a \tag{10}$$

Because we have the drag coefficient for the bed from the bare ditch line experiment, we were able to obtain an estimate for the effective shear stress acting on additional roughness elements. Writing Equation (10) as a force balance:

$$\rho_w g R S = \tau_g + \tau_a$$
$$\Rightarrow \rho_w g R S = \rho_w C_B U^2 + \rho_w C_A U^2$$
$$\Rightarrow C_A = \frac{gRS}{U^2} - C_B \tag{11}$$

where C_A is the drag coefficient on the additional roughness elements. Again, because g is a known constant, C_B was obtained in the bare ditch experiment, and R, S, and U were measured in the field, we could obtain a value for C_A. Knowing the values for C_B and C_A allowed us to obtain Manning's n values for the sediment grains and the additional roughness elements.

6.2.3 Calculating Manning's n for Sediment Grains

To calculate Manning's n for sediment grains, we took Equation (9) and re-wrote it in the form of Chezy's equation:

$$U = C\sqrt{RS} \qquad (Chezy)$$

$$U = \underbrace{\sqrt{\frac{g}{C_B}}}_{C}\sqrt{RS} \qquad (12)$$

where the C in Chezy's equation is a constant and becomes $\sqrt{\frac{g}{C_B}}$ in Equation (12). Again, U is the field-measured velocity, R is the calculated hydraulic radius, and S is the slope of the ditch.

We then re-wrote Chezy's equation as Manning's equation:

$$\mathrm{U} = \underbrace{\frac{1}{n}R^{1/6}}_{C}\sqrt{RS} \qquad (Manning)$$

Here, C is equivalent to $\frac{1}{n}R^{1/6}$. We used this information to then calculate Manning's n for sediment grains in terms of C_B:

$$\sqrt{\frac{g}{C_B}} = \frac{1}{n_B}R^{1/6}$$

$$\Rightarrow n_B = \sqrt{\frac{C_B}{g}}R^{1/6} \qquad (13)$$

6.2.4 Calculating Manning's n for Additional Roughness Elements

Using a similar method to 6.2.3, we got Manning's n for additional roughness elements. Taking Equation (11), we re-wrote it as:

$$U = \sqrt{\frac{g}{C_A + C_B}}\sqrt{RS}$$

$$\Rightarrow U = \underbrace{\sqrt{\frac{g}{C_T}}}_{C}\sqrt{RS} \qquad (14)$$

For ease of calculation, we defined $C_A + C_B$ as C_T. Setting C in Equation (14) equal to C in Manning's equation, we got:

$$\sqrt{\frac{g}{C_T}} = \frac{1}{n_T}R^{1/6}$$

$$\Rightarrow n_T = \sqrt{\frac{C_T}{g}}R^{1/6} \qquad (15)$$

where C_T is the drag coefficient for the bed and additional roughness elements and n_T is the total Manning's n. To get Manning's n for the additional roughness elements, we simply subtracted n_B from n_T:

$$n_A = n_T - n_B \qquad (16)$$

6.3 Preliminary Data Analysis Results

Below we present values from our preliminary data analyses (*Table 6.1–Table 6.4*). We have included the hydraulic radii, drag coefficients, and Manning's n values for each experimental run. All values have been calculated using the field-measured velocity, U, and two field-measured discharge values, Q_1 and Q_{obs}, which are discharge values based on the salt tracer data and the measured outflow at the water truck, respectively. Further discussion among the project team is required to finalize the analyses of the collected data. The second year of this parameterization experiment will be carried out in the next biennium, and the methodology and analyses will continue to be refined in the meantime.

In *Table 6.1* preliminary values for disturbed bare ditch drag coefficients and Manning's n values (KID-14 Bare) are presented and preliminary values for undisturbed bare ditch drag coefficients and Manning's n values (MEL-13 Bare). The distinction is made between disturbed bare ditch and undisturbed bare ditch because of the initial conditions at each site: at KID-14, the ditch was smoothed right before the experiment whereas MEL-13 had no smoothing; consequently, MEL-13 represents an "armored" bare ditch condition where fines have been winnowed out leaving coarser material (Luce and Black, 2001). Given the low grass cover in MEL-12, we expected similar behavior there.

Table 6.1 *Table of hydraulic radii, drag coefficients and Manning's n values calculated using two different discharge values: Q_1 and Q_{obs}, where Q_1 is the discharge calculated based on the salt tracer data, and Q_{obs} is the discharge measured at the water truck outflow. NaN = Not a number (i.e., no value).*

Experimental Run ID	R_{Q1} (m)	R_{Qobs} (m)	$C_{B,Q1}$	$C_{B,Qobs}$	$n_{B,Q1}$	$n_{B,Qobs}$
KID-14 Bare 15A	0.014	0.013	0.131	0.125	0.057	0.055
KID-14 Bare 15B	0.014	NaN	0.122	NaN	0.054	NaN
KID-14 Bare 25A	0.017	0.013	0.062	0.047	0.040	0.034
KID-14 Bare 25B	0.018	NaN	0.083	NaN	0.047	NaN
KID-14 Bare 40A	0.019	0.019	0.050	0.050	0.037	0.037
MEL-13 Bare 15A	0.016	0.014	0.378	0.324	0.099	0.089
MEL-13 Bare 15B	0.017	0.013	0.402	0.311	0.103	0.087
MEL-13 Bare 25A	0.020	0.018	0.324	0.287	0.095	0.087
MEL-13 Bare 25B	0.020	0.017	0.324	0.285	0.094	0.087
MEL-13 Bare 40A	0.025	0.021	0.268	0.224	0.089	0.079
MEL-13 Bare 40B	0.030	0.021	0.321	0.224	0.101	0.079

In *Table 6.2*, preliminary values are presented for the drag coefficients and Manning's n values of wattles added to the ditch (KID-14 Wattles and MEL-13 Wattles). Because we carried out the bare ditch experiment and wattles experiment in the same ditch, we assume that the additional roughness values can be calculated as presented in section 6.2. A much higher wattle density was used at MEL-13 (19 wattles) than KID-14 (10 wattles) because the KID-14 installation left more length unponded than desired and because MEL-13 was steeper, requiring more wattles per unit length. Total and additional roughness values are consequently much greater.

Table 6.2 *Table of hydraulic radii, total drag coefficients, total Manning's n values and Manning's n values for additional roughness elements calculated using two different discharge values for wattled field sites: Q_1 and Q_{obs}, where Q_1 is the discharge calculated based on the salt tracer data, and Q_{obs} is the discharge measured at the water truck outflow. NaN = Not a number (i.e., no value).*

Experimental Run ID	R_{Q1} (m)	R_{Qobs} (m)	$C_{T,Q1}$	$C_{T,Qobs}$	$n_{T,Q1}$	$n_{T,Qobs}$	$n_{A,Q1}$	$n_{A,Qobs}$
KID-14 Wattles 15B	0.039	0.026	5.343	3.596	0.429	0.330	0.375	NaN
KID-14 Wattles 25A	0.045	0.035	4.884	3.836	0.420	0.358	0.380	0.324
KID-14 Wattles 40A	0.056	0.043	4.320	3.342	0.410	0.346	0.373	0.309
MEL-13 Wattles 15A	0.032	0.037	13.403	15.181	0.660	0.717	0.561	0.628
MEL-13 Wattles 40A	0.052	0.050	12.512	12.144	0.690	0.676	0.600	0.597

In *Table 6.3* and *Table 6.4*, preliminary values are presented for the total drag coefficients and Manning's n values of each of the ditches (KID-15 Grassed, MEL-12 Grassed, and KID-39 Graveled). For these sites, the totals of these values are presented because these experiments were carried out in ditches for which we do not have values for the bare conditions. Though MEL-12 was left undisturbed, and grass seed was applied in the previous year, the grass coverage that existed at the time of the study was very sparse, so the site conditions may have represented "armored" conditions reflecting roughness from the coarse material that was not transported by the preceding runoff events more than roughness from a canopy of grass stems. The similarity in roughness value estimates to those at MEL-13 supports this perspective.

Further research and discussion are required to determine the partitioning of roughness values for each different attribute (i.e., sediment grains vs. additional treatment-related roughness).

Table 6.3 *Table of hydraulic radii, total drag coefficients and total Manning's n values calculated using two different discharge values for grassed field sites: Q_1 and $Q_{obs,}$ where Q_1 is the discharge calculated based on the salt tracer data, and Q_{obs} is the discharge measured at the water truck outflow.*

Experimental Run ID	R_{Q1} (m)	R_{Qobs} (m)	$C_{T,Q1}$	$C_{T,Qobs}$	$n_{T,Q1}$	$n_{T,Qobs}$
KID-15 Grassed 15A	0.034	0.032	9.792	9.113	0.568	0.542
KID-15 Grassed 15B	0.027	0.034	9.432	12.176	0.536	0.636
KID-15 Grassed 25A	0.033	0.043	7.616	9.901	0.499	0.594
KID-15 Grassed 25B	0.035	0.048	13.756	18.762	0.677	0.833
KID-15 Grassed 40A	0.042	0.043	4.041	4.119	0.379	0.384
KID-15 Grassed 40B	0.041	0.043	4.061	4.273	0.378	0.391
MEL-12 Grassed 15A	0.012	0.010	0.368	0.309	0.093	0.082
MEL-12 Grassed 15B	0.012	0.010	0.416	0.370	0.098	0.091
MEL-12 Grassed 25A	0.016	0.014	0.385	0.329	0.100	0.090
MEL-12 Grassed 25B	0.017	0.014	0.444	0.381	0.107	0.097
MEL-12 Grassed 40A	0.018	0.018	0.280	0.273	0.087	0.085
MEL-12 Grassed 40B	0.018	0.018	0.277	0.284	0.086	0.087

Table 6.4 *Table of total drag coefficients and total Manning's n values calculated using two different discharge values for graveled field site: Q_1 and $Q_{obs,}$ where Q_1 is the discharge calculated based on the salt tracer data, and Q_{obs} is the discharge measured at the water truck outflow.*

Experimental Run ID	R_{Q1} (m)	R_{Qobs} (m)	$C_{T,Q1}$	$C_{T,Qobs}$	$n_{T,Q1}$	$n_{T,Qobs}$
KID-39 Gravel 25A	0.035	0.033	2.925	2.715	0.313	0.298
KID-39 Gravel 40A	0.036	0.030	0.758	0.627	0.160	0.141

7 Micro-Topography Experiment

Shallow overland flow is a common occurrence on mainline logging roads during rainfall. Micro-topographic features on these roads affect the way in which water flows and, thus, affect the disposition of the water and the sediment carried thereby. The objective of this parameterization experiment is to characterize the evolution of these micro-topographic features using two kinds of high-resolution mapping technology: 1) unmanned aerial vehicles (UAVs) with structure-from-motion (SfM) technologies; and 2) terrestrial LiDAR scanning (TLS). These mapping technologies yield repeat high-resolution digital elevation models (DEMs) and will allow us to further understand how the micro-topographical evolution of roads affects sediment production. Final DEM products will be used for refining, calibrating, and testing the sediment transport model; analyzing the covariance of micro-topographical evolution—and thus, sediment production—with variables such as traffic and rainfall; and extracting sediment yield estimates from the road surface by differencing elevations through time.

7.1 Background and Motivation

The characteristics of shallow water flow on forest roads have a large impact on sediment transport. If water flows diffusely, little erosion occurs, but where water concentrates in rills and ruts, shear stress increases, and more sediment is transported. If sediment-laden water flows off the road tread into the ditch, ditch line best management practices (BMP) can act to moderate the sediment. However, if the water flows along the road—down the road tread—it may deliver to the stream untreated. Ultimately, the way in which water flows is controlled by micro-topographic features of the road surface. Changes to the road micro-topography over time may be subtle but are likely to be critical to BMP effectiveness.

Understanding and accurately modeling micro-topographic evolution of the road surface, particularly the formation of concentrated flow paths (i.e., rills and ruts), is critical for the following reasons:

1. The formation of rills and ruts amplifies erosion and transport due to the shear stress occurring in concentrated flow being greater than that which occurs in diffuse overland flow prior to rill development.
2. Higher shear stress in rills and ruts more effectively entrains and transports both fine and coarse sediment in greater volumes, altering the size distribution of sediment at the basin outlet.
3. Wheel ruts shift flow that was destined to be concentrated flow in a ditch—where vegetation and other BMP can operate to reduce grain shear stress—onto the road surface where little mitigation of concentrated flow can occur.

Representing the links between micro-topographic evolution and sediment characteristics of the road surface material, grading, traffic, climate, and lithology will have direct implications on road maintenance and traffic control. Additionally, having the capacity to realistically model the evolution of micro-topographic features and sediment yields concurrently will enhance model performance and credibility for producing large, modeled data sets.

In the past, erosion models have been tested with laboratory-scale experiments involving close-range photogrammetry and LiDAR mapping (Hancock and Willgoose, 2001; Jomaa et al., 2010; Cuomo et al., 2016). This experiment will use similar technology—UAVs, SfM, and TLS—albeit at a larger scale.

7.2 Methods

This parameterization experiment is being conducted over a two-year period at two field sites that have similar physical characteristics (KID-13 and MEL-14) and has two main types of surveys: 1) dual-method surveys using TLS technology and UAV technology; and 2) UAV-only surveys. This experiment began in November 2020 and will continue for two years, each in two phases. Each phase consists of two dual-method surveys and two UAV-only surveys. The first phase occurs during the fall and winter months each year after the road has been re-rocked and re-graded prior to the rainy season. The second phase occurs during the spring and summer months each year after the road has been re-graded post-rainy season.

7.2.1 General Setup

Both the TLS and UAV portions of the surveys require ground control points (GCP). These GCPs are used to ensure high accuracy and high precision repeat surveys. Two "permanent" benchmarks and 24 "normal" benchmarks have been installed at each field site. The two permanent benchmarks exist to maintain ground truthing in the case that the normal benchmarks move during road work.

Permanent Benchmarks:

- Compacted instrument platforms off to the side of the road that do not change through time.
- Approximately 100 feet apart with line of sight to the road prism and to each other.
- Precise locations were measured for each of these benchmarks at the outset of the experiment and will be repeated during each dual-method survey to ensure that the benchmarks did not move.

Normal Benchmarks:

- 10-inch nails driven into the sides of the road prism and spray painted with an "X" and benchmark number.
- All normal benchmarks are on the side of road prism due to UAV flight constraints, as well as traffic constraints.
- These benchmarks were located and installed during first dual-method survey.
- Precise locations are determined for these benchmarks during each dual-method survey.

7.2.2 Terrestrial LiDAR Scanning

The TLS surveys occur 8 times throughout the entire experiment: 1) immediately after the first re-rocking and re-grading occur in each year; 2) immediately before the second re-grading each year; 3) immediately after the second re-grading occurs each year; and 4) at the end of each year. Tasks include:

- Obtaining locations for permanent benchmarks in local coordinate system using a Trimble SX-10 scanning total station.
- Carrying out a full TLS survey using a Trimble SX-10 scanning total station.
- Obtaining locations for normal benchmarks in local coordinate system based on permanent benchmarks using a Trimble SX-10 scanning total station.

7.2.3 Unmanned Aerial Vehicles

The UAV surveys are scheduled to occur 24 times throughout the experiment: 1) every time the dual-method survey is carried out (8 times) and 2) twice between each dual-method survey. The UAV survey is conducted by one person.

- Run UAV survey:
    - Use DJI Phantom 4 Pro Drone.
    - Manual control.
    - Approximately 500-600 photos per site to ensure full coverage.
        - Consecutive photos have approximately 70% overlap.
    - Camera nadir and at an angle.

So far, three dual-method surveys and two UAV-only surveys have been carried out. The entire first phase of year 1 and the first dual-method survey for the second phase of year 1 have been completed. The results presented in the following sections include only those surveys completed during the first phase of this first year.

7.3 Survey Results

Below, preliminary results are presented from the first phase of Year 1 of this experiment at both the volcanic lithology site, KID-13, and the siltstone lithology site, MEL-14. Figure 7.1 demonstrates results from the KID-13 SfM surveys done on 11/09/2020 (left column), 02/08/2021 (middle column), and 04/06/2021 (right column). Similarly, Figure 7.2 demonstrates results from the MEL-14 SfM surveys done on 12/03/2020 (left column), 02/24/2021 (middle column), and 04/12/2021 (right column). In both figures, the top row of results show the processed digital surface model overlaying an orthomosaic image of the road surface, and the bottom row of results show the processed hillshade of the digital surface model.

The first survey at KID-13, carried out on November 9, 2020, was a dual-method survey and occurred a week after the road had been graded due to inclement weather. In this initial survey, new wheel ruts are starkly defined, which demonstrates that the initiation of ruts occurs quickly after road grading. As time progresses, gravel is scattered to the sides of the road, and the wheel ruts begin to expand likely due to the stochasticity of traffic location on the road.

The first survey at MEL-14, carried out on December 3, 2020, was also a dual-method survey and occurred only two days after the road had been graded. In this December 3 survey, new wheel ruts are not as starkly defined as in Figure 7.1. This is likely because: 1) the survey occurred soon after the road was graded; 2) not much traffic was present the road segment; or 3) a combination of 1 and 2. In the February 8 survey, the wheel ruts are much more defined. The April 12 survey is shown here for completeness but is unfortunately unusable due to unforeseen grading carried out by landowners—the road had been heavily used and required quick patchwork. Going forward, communication between the project team and the landowners will be clearer.

The second dual-method survey at KID-13 of Year 1, phase 1 was carried out on May 13, 2021, and served as the final survey prior to Year 1, phase 2. Those results are currently being processed. Because of the unanticipated road grading at MEL-14, the second dual-method survey of Year 1, phase 1 was not carried out there.

Phase 2 of the first year at KID-13 began on June 4, 2021, which was when the road was re-graded. At MEL-14, the first dual-method survey of phase 2 occurred on June 3, 2021, which was also the same date as road grading. The data for these surveys will be processed in the next biennium.

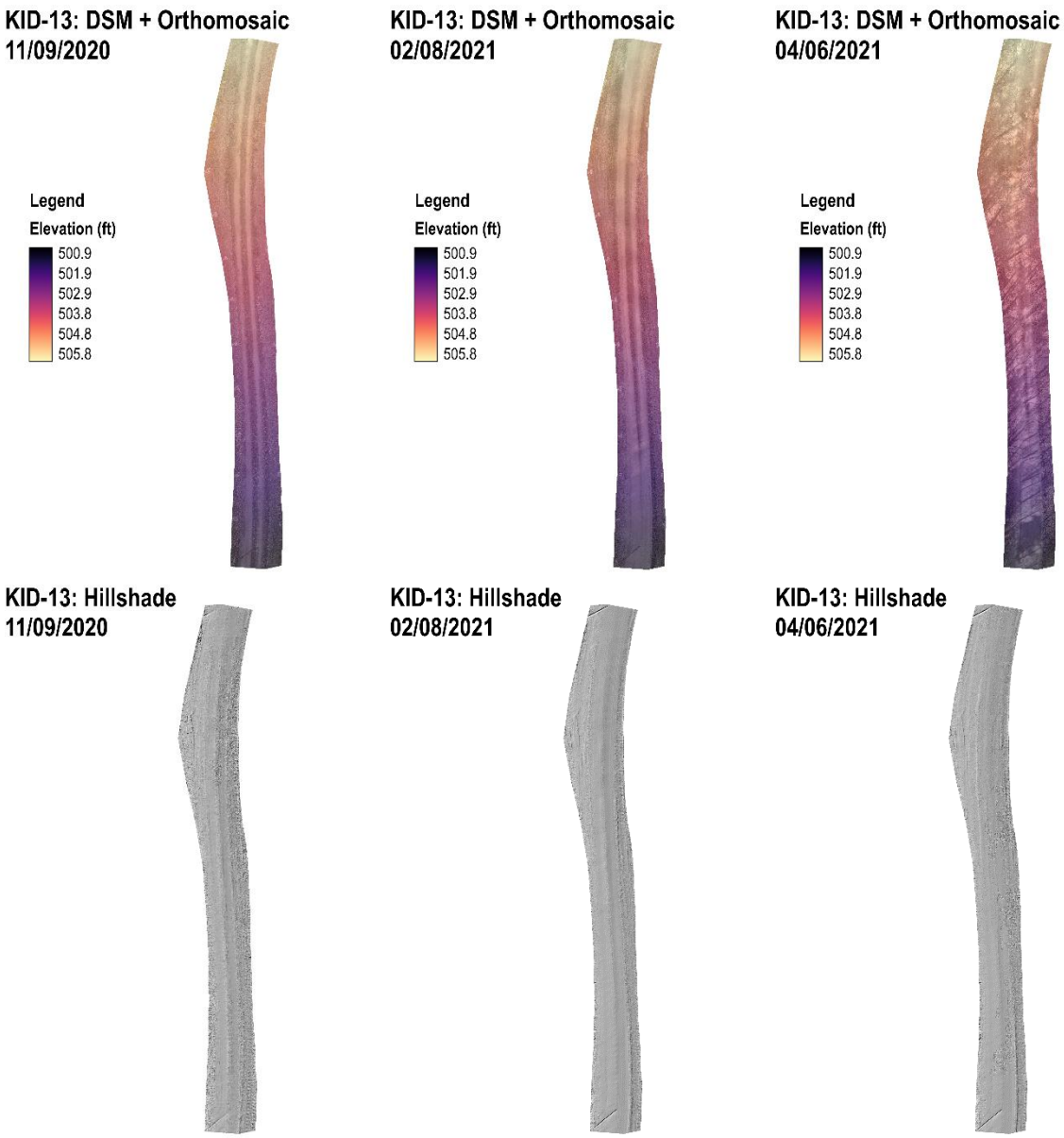

Figure 7.1 *Maps of processed micro-topography data at KID-13 for surveys on 11/09/2020, 02/08/2021, and 04/06/2021. KID-13: DSM & Orthomosaic is the digital surface model overlaying an orthomosaic image of the road surface. KID-13: Hillshade is a hillshade of the digital surface model and shows more detail of the road surface. As time progresses, gravel is scattered to the sides of the road, and the initially stark wheel ruts begin to expand likely due to the stochasticity of traffic location on the road.*

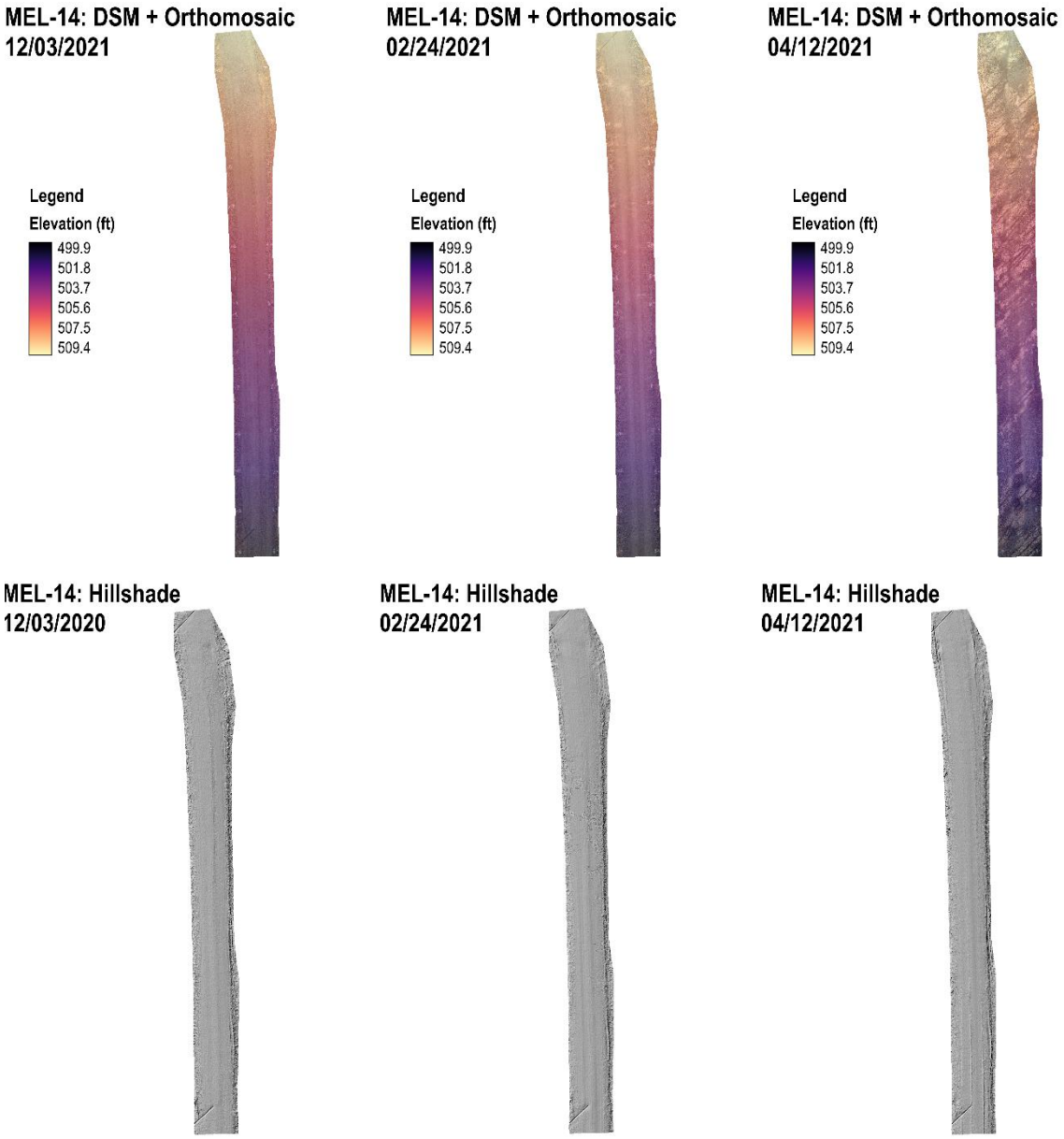

Figure 7.2 *Maps of processed micro-topography data at MEL-14 for surveys on 12/03/2020, 02/24/2021, and 04/12/2021. MEL-14: DSM & Orthomosaic is the digital surface model overlaying an orthomosaic image of the road surface. MEL-14: Hillshade is a hillshade of the digital surface model and shows more detail of the road surface. As time progresses, gravel is scattered to the sides of the road, and wheel ruts begin forming. Note that the 04/12 survey is shown here for completeness.*

7.4 Future Analysis

Going forward, the results from these surveys—specifically, the high-resolution digital surface models—will be used for: 1) refining, calibrating, and testing the sediment transport model; 2) analyzing the covariance of micro-topographical evolution with variables such as traffic and rainfall; and 3) estimating sediment yields from the road surface through differencing of DEMs between subsequent surveys.

1. With such high resolution (millimeter scale), the DEMs are allowing us to accurately model the micro-topography and its changes. This will lead to higher accuracy in the output of the model being developed for this project. We will be able to run the model using the initial survey DEM as input and compare our model output to the intermediate or final surveys.
2. We will be able to look at how the micro-topography changes in relation to other variables such as rainfall and traffic. We will perform an analysis of covariance (ANCOVA) to examine these relationships.
3. We can difference two DEMs (initial and later in time) after ensuring they have the same extent, resolution, and projection, and ultimately obtain an approximate volume of displaced sediment which can be compared to field data/model output.

8 References

Black, T. A. and Luce, C. H., 2013. Measuring Water and Sediment Discharge from a Road Plot with a Settling Basin and Tipping Bucket. Gen. Tech. Rep. RMRS-GTR-287. Fort Collins, CO: U.S. Department of Agriculture, Forest Service, Rocky Mountain Research Station.

CMER, 2017. Empirical and Modeled Evaluation of Forest Road BMP Effectiveness in Western Washington, Study Plan.

Cuomo, S. et al., 2016. Experimental evidences and numerical modelling of runoff and soil erosion in flume tests. In: *Catena* 147, pp. 61-70.

Dubé, K., et al., 2010. Washington road sub-basin scale effectiveness monitoring first sampling event (2006-2008) report. Cooperative Monitoring, Evaluation and Research Report CMER 08-801. Washington Department of Natural Resources. Olympia, Washington.

Einstein, H. A. and Barbarossa, N. L., 1952. River channel roughness. In: *Transactions of the American Society of Civil Engineers 117*(1), pp. 1121–1132.

Foltz, R., and Truebe, M., 2003. Locally available aggregate and sediment production. In: *Transportation Research Record, 1819*(1), pp. 185–193.

Govers, G., 1992. Evaluation of transporting capacity formulae for overland flow, pp. 243–273, In: *Overland Flow Hydraulics and Erosion*. UCL Press, London. Edited by Parsons, A. J. and Abrahams, A. D.

Hancock, G., and Willgoose, G., 2001. Use of a landscape simulator in the validation of the SIBERIA Catchment Evolution Model: Declining equilibrium landforms. In: *Water Resources Research, 37*(7), pp. 1981–1992

Hirano, M., 1971. Riverbed degradation with armoring. In: *Trans. Jpn. Soc. Civ. Eng.* 3, pp. 194–195.

Istanbulluoglu, E. et al., 2003. A sediment transport model for incision of gullies on steep topography. In: *Water Resources Research 39*(4).

Jomaa, S. et al., 2010. Effect of raindrop splash and transversal width on soil erosion: laboratory flume experiments and analysis with the Hairsine–Rose model. In: *Journal of Hydrology, 395*(1), pp. 117-132.

Luce, C. H. and Black, T. A., 1999. Sediment Production from Forest Roads in Western Oregon. In: *Water Resources Research, 35*(8), pp. 2561-2570.

Luce, C. H. and Black, T. A., 2001. Spatial and Temporal Patterns in Erosion from Forest Roads, pp. 165-178, In: *Influence of Urban and Forest Land Uses on the Hydrologic-Geomorphic Responses of Watersheds*. American Geophysical Union, Washington, DC. Edited by Wigmosta, M. W. and Burges, S. J.

Manga, M. and Kirchner, J. W., 2000. Stress partitioning in streams by large woody debris. In: *Water Resources Research* 36(8), pp. 2373–2379.

van Meerveld, H. J. et al., 2014. Controls on sediment production from an unpaved resource road in a Pacific maritime watershed. In: *Water Resources Research*, 50, pp. 4803–4820, doi:10.1002/2013WR014605.

MesoWest, University of Utah, https://mesowest.utah.edu, data accessed 1 July 2020.

PRISM Climate Group, Oregon State University, http://prism.oregonstate.edu, data accessed 5 July 2017.

Reid, L., and Dunne, T., 1984. Sediment production from forest road surfaces. In: *Water Resources Research, 20*(11), pp. 1753–1761.

Rhee, H. et al., 2018. Traffic-Induced Changes and Processes in Forest Road Aggregate Particle-Size Distributions. In: *Forests, 9*(4), p. 181.

Suttle, K. B. et al., 2004. How fine sediment in riverbeds impairs growth and survival of juvenile salmonids. In: *Ecological Applications,* 14, pp. 969–974.

Ziegler, A. et al., 2001. Interstorm surface preparation and sediment detachment by vehicle traffic on unpaved mountain roads. In: *Earth Surface Processes and Landforms: The Journal of the British Geomorphological Research Group, 26*(3), pp. 235–250.